
Article:
Hooper, T.E. orcid.org/0000-0002-8538-8483 and Sinclair, D.C. orcid.org/0000-0002-8031-7678 (2024) Structural, dielectric, and conduction behaviour of A-site deficient SrxNa1−2xNbO3 ceramics. Journal of Materials Chemistry C, 12 (33). pp. 12992-13001. ISSN 2050-7526

https://doi.org/10.1039/d4tc02433h

Structural, Dielectric, and Conduction Behaviour of A-site deficient $Sr_xNa_{1-2x}NbO_3$ Ceramics

Thomas E. Hooper[1] and Derek C. Sinclair

Department of Materials Science and Engineering, Sir Robert Hadfield Building, University of Sheffield, Mappin Street, Sheffield S1 3JD, UK

Abstract *The crystallographic and electrical properties of A-site deficient $Sr_xNa_{1-2x}NbO_3$ (x= 0.00, 0.05, 0.10, 0.15, 0.20, and 0.25) perovskites have been studied by X-ray diffraction, scanning electron microscopy, dielectric spectroscopy, impedance spectroscopy and polarisation against electric field loops. Despite complexities in the microstructural evolution due to the formation of $NaNb_3O_8$ liquid phase, the crystallographic and dielectric properties show much clearer trends. The introduction of A-site vacancies shows an almost linear expansion of the pseudo-cubic unit cell volume of ~ 0.05 $Å^3$/at% stabilising the ferroelectric $P2_1ma$ Q-phase. Compositions x > 0.10 show increasingly relaxor-like behaviour in the dielectric properties and impedance spectroscopy shows increasing conductivity and tan δ values associated with predominantly electronic conduction from x = 0.05 to 0.25. Measurements in N_2 at 600 °C show progressively n-type behaviour with increasing levels of A-site vacancies due to the increased tendency to lose under-bonded O^{2-} ions and therefore partially reduce some Nb^{5+} to Nb^{4+} ions. Although it is not possible to fully establish the electrical properties of our undoped $NaNbO_3$ ceramics, we propose they contain mixed ionic-electronic behaviour with the clear presence of a weak n-type dependent grain boundary contribution to the total conductivity.*

Keywords: Sodium niobate, perovskites, defect chemistry, dielectric properties, conductivity

[1] Corresponding author: thomas.elliot.hooper@gmail.com

1. Introduction

Sodium niobate ($NaNbO_3$) is a material of interest both academically as a vessel for understanding the phenomenology of antiferroelectric materials [1], and technologically as a material for applications in energy storage [2, 3], photocatalysis [4, 5], and as an end member component for piezoelectric actuation [6, 7]. The crystallographic properties of $NaNbO_3$ are somewhat more complex than other perovskite counterparts, exhibiting seven polymorphs from ~ -100 °C to ~640 °C. Below -100 °C, $NaNbO_3$ exhibits a rhombohedral *R*3*c* ferroelectric (FE) phase. On heating this changes to a series of orthorhombically distorted cells: antiferroelectric (AFE) *Pbcm* ≤ 360 °C ≤ AFE *Pnmm* ≤ 480 °C ≤ paraelectric (PE) *Pnmm* ≤ 520 °C ≤ PE *Ccmm*, before transforming into the higher symmetry tetragonal PE P4/mbm at 575 °C and cubic PE *Pm*3*m* at 640 °C [2, 8]. Although the room temperature polymorph of $NaNbO_3$ is generally accepted to be an AFE *Pbcm* structure referred to as P-phase, it is also accepted that this can co-exist with unit cells associated with the 'forced ferroelectric' $P2_1ma$ space group referred to as Q-phase [9]. The degree of coexistence between these phases varies greatly and has been shown to depend on stoichiometry, grain size and/or morphology, and sintering temperatures [10, 11].

Like many perovskite systems, $NaNbO_3$ can readily form solid solutions with other 1:5 perovskites such as $KNbO_3$ [6, 7], 2:4 perovskites such as $BaTiO_3$ [3, 12-14] and $PbTiO_3$ [15], and 3:3 perovskites such as $BiFeO_3$ [16, 17]. Unlike some perovskite systems such as $BaTiO_3$, $NaNbO_3$ shows relative ease in A-site vacancy generation, forming compositionally wide solid solutions with $Bi_{1/3}NbO_3$ [18, 19] and $CaNb_2O_6$ [20, 21], and even full solid solutions with $La_{1/3}NbO_3$ [22] and $Nd_{1/3}NbO_3$ [23, 24]. Lopez et al. [25] were even able to fabricate heavily A-site deficient $Na_{0.6}NbO_3$ whilst retaining a stable perovskite with P→Q. This not only provides an interesting avenue of research with regards to A-site vacancies in perovskites, but also the possibility to exploit technological capabilities that come with the generation of these vacancies and the subsequent inducing of relaxor-like behaviour.

Despite the phase diagrams of $SrNb_2O_6$-$NaNbO_3$ being constructed in the early and late 1970s [26], very few studies have been conducted to probe the perovskite region of this phase diagram with nomenclature $Sr_xNa_{1-2x}NbO_3$. Torres-Pardo et al. [27, 28] used a combination of diffraction methods and high-resolution electron microscopy to probe local structure correlations to the dielectric behaviour in $Sr_xNa_{1-2x}NbO_3$ (x = 0.10, 0.15, 0.20). The authors reported two key findings: 1) the observation of progressive ferroelectric stabilisation with the disappearance of P-type structural domains in favour of a Q-like phase; 2) the reduction of domain size from ~100 to ~10 nm to a few unit cells for x = 0.10, 0.15, and 0.20, respectively. The introduction of A-site vacancies results in an increase in domain wall density to counteract

local mechanical stresses, which in turn reduces the coherence length of the domains and induced relaxor behaviour in the dielectric properties.

There have been various reports using impedance spectroscopy (IS) to obtain the conduction properties of undoped $NaNbO_3$ but the magnitudes of the conductivity and activation energy, E_a, values vary dramatically depending on how the samples were processed and how the IS data were measured. Lei et al [18] prepared samples by solid state processing with sintering of ceramics at 1170 ^oC for 5 - 30 hr and obtained a linear Arrhenius plot for the bulk conductivity over the range ~ 450 – 700 ^oC with E_a = 1.75 eV which would be consistent with intrinsic electronic conduction. In contrast, G. Gouget et al [29] used spark plasma sintering at 900 ^oC followed by a reoxidation process to prepare undoped $NaNbO_3$ ceramics and reported linear Arrhenius behaviour for the total conductivity over the range 400 to 900 ^oC with E_a ~ 0.8 eV. They attributed the conductivity to be exclusively ionic, based on mixed Na^+ and O^{2-} ions and used oxide-ion blocking yttria-stabilised zirconia electrodes to estimate transport numbers of t_{Na+} ~ 0.88 and t_{o2-} ~ 0.12 between 350 – 700 ^oC.

The work presented here is designed to complement previous work on this solid solution by expanding on the dielectric properties, and to provide an additional perspective on the conduction behaviour of doped and undoped $NaNbO_3$ by means of impedance spectroscopy in air and N_2.

2. Experimental Procedure

Commercially available reagents of $SrCO_3$ (Sigma Aldrich, 99.9%), Na_2CO_3 (Sigma Aldrich, 99.5%), and Nb_2O_5 (Alfa Aesar, 99.95%) were dehydrated overnight and weighed stoichiometrically to form $Sr_xNa_{1-2x}NbO_3$ (x = 0.00, 0.05, 0.10, 0.15, 0.20, 0.25), (see SI section 1 for more details). Powders were ball milled in isopropanol for 24 hours, dried and sieved, and underwent two calcinations at 800 ^oC for 6h with intermediate ball milling, (see SI section 2 for more details). Powders were uniaxially pressed at 12.5 MPa into 10 mm diameter pellets and cold isostatically pressed at 32 kpsi for 5 minutes. Pellets were buried in powder of the same composition and sintered at 1340 ^oC for 5 h.

X-ray diffraction (XRD) was performed on crushed sintered bulk samples annealed at 600°C for 1 hour (cooling rate = 0.8 °C.min^{-1}). Data were collected using monochromatic molybdenum $K\alpha_1$ (λ=0.7096 Å) radiation, measured using a STADI P diffractometer with a Mythen detector (STOE, Germany) and step size 0.015°. Rietveld refinements were conducted for the diffraction patterns using GSAS-II software [30] where refined parameters included lattice

parameters, atomic coordinates, site occupancies, thermal parameters, microstrain and crystallite size.

Ceramic microstructures were analysed using an Inspect F50 scanning electron microscope (FEI, Netherlands) with accelerating voltage of 20 kV and working distance of 10 mm. Samples were polished beforehand using diamond paste (Beuhler) from 6 to 1 μm and thermally etched at 1140 °C for 15 minutes before sputter coating a 5 nm Au layer to avoid charging.

For electrical measurements, samples were ground and polished using SiC paper and electroded using fire-on Au paste (SunChemical, UK) at 850 °C for 2 h. High temperature Dielectric Spectroscopy (DS) and Impedance Spectroscopy (IS) analysis were carried out using an Agilent E4980A Precision LCR Meter. IS measurements were carried out using a 0.1 V *ac* signal from 20 Hz to 1 MHz at 25 °C intervals with 20 minutes dwell time. Subambient DS analysis was carried out using an Agilent E4980A Precision LCR Meter connected to a Cryodrive 1.5 cryocooler (Oxford Instruments, UK). High temperature and subambient DS data was stitched together at 25 °C to form a high and low temperature continuous plot. Atmospheric IS measurements were carried out on a Solartron SI 1260 impedance analyser using a 0.1 V *ac* signal from 20 Hz to 1 MHz. Measurements were first carried out in air at ~ 600 °C before being flushed with flowing N_2 overnight and running another measurement.

High voltage measurements were carried out using a Precision LC Analyser (Radiant, USA) connected to a Trek 5/80 high voltage amplifier (Trek, USA) using a 1 Hz signal on fully electroded samples on the top and bottom surfaces. Samples were submerged in silicone oil to increase the dielectric breakdown voltage and prevent arcing.

3. Results & Discussion

Stacked XRD patterns for all compositions, and pseudo-cubic lattice parameters and unit cell volume against composition are shown in Figure 1 (see SI section 3 for more details) and refined parameters are shown in Table 1. All samples $0 \leq x \leq 0.20$ show single phase perovskite whereas x = 0.25 displays a small amount of tetragonal tungsten bronze (TTB) with nomenclature $Sr_2NaNb_5O_{15}$, demonstrating a solid solution limit between 0.20 and 0.25; concordant with the phase diagram from Tang et al. [26]. Although the solid solution limit is in agreement, there is a difference in the $NaNbO_3$ polymorph at high Sr^{2+} contents with Tang et al. claiming a cubic $NaNbO_3$ polymorph at room temperature from ~ $0.15 < x < 0.22$ whereas XRD patterns for x = 0.20 and x = 0.25 in this study could be indexed according to an orthorhombic $P2_1ma$ space group. The argument against a cubic $NaNbO_3$ symmetry is discussed in more detail later in this manuscript. x = 0.00 and 0.05 can be indexed according

to an antiferroelectric *Pbcm* (P) space group due to the presence of (113) and {331} reflections at ~13.1° and ~24.6° 2θ, respectively (Mo-Kα source). x = 0.10, 0.15, 0.20, and 0.25 can be indexed to the ferroelectric $P2_1ma$ (Q) space group consistent with Torres-Pardo *et al*. [27, 28].

All tilt components are retained with composition as shown in Figure 1(b), however the reflections become more diffuse with increasing A-site vacancy concentration and breaking of long-range order. Torres-Pardo et al. [27, 28] used TEM to show that with increasing Sr^{2+} (and subsequently A-site vacancy) concentration, a structural change from long-range Q-phase ordering to short-range clusters of Q phase occurs. Arguably the out-of-phase component (B) is the most retained with the in-phase tilting components (A and D) becoming almost too diffuse to detect. This is contrary to Levin et al. [19] in $Bi_xNa_{1-3x}NbO_3$ where increasing Bi and A-site vacancy concentration lead to undetectable out-of-phase tilting. This clearly suggests that the influence of A-site vacancies alone doesn't dictate the structural variations and that the ionic radii and preferred co-ordination environments of the A-site dopant cations also play a significant role.

Figure 1(c) shows the pseudo-cubic (PC) lattice parameters where $a_{PC} = a/\sqrt{2}$, $b_{PC} = b/\sqrt{2}$, $c_{PC} = c/4$ when converting from *Pbcm* (x = 0.00 & 0.05) and $a_{PC} = a/\sqrt{2}$, $b_{PC} = b/2$, $c_{PC} = c/\sqrt{2}$ when converting from $P2_1ma$ (x = 0.10 – 0.25). PC c and a/b ($P2_1ma$/*Pbcm*) parameter displays an almost linear expansion with composition whist PC b/a ($P2_1ma$/*Pbcm*) decreases up to x = 0.15 before following an almost linear trend similar to other parameters. This behaviour is also demonstrated in the refined pseudo-monoclinic tilt angle which tend to 90° with increasing A-site vacancy concentration (SI section 3, Figure S7). However the retention of the out-of-phase and in-phase tilting components shown in Figure 1(b) is evidence against tetragonal symmetry as no tilting components would be observed in the *P*4/*mbm* space group.

PC unit cell volume increases almost linearly with composition as shown in Figure 1(d) by ~0.05 $Å^3$/at%. This behaviour is as expected for two reasons; the substitution of Na^+ (1.39 Å [31]) by larger Sr^{2+} (1.44 Å [31]) ions, and the increase in coulombic repulsion from O^{2-} ions which act to expand the unit cell due to increasing A-site vacancies and subsequent loss of electrostatic shielding provided by cations. Aso et al. [20] reported a systematic decrease in unit cell parameters between $0.00 \leq x \leq 0.15$ for $Ca_xNa_{1-2x}NbO_3$, demonstrating that the relative size of the A-site substitution dominates changes in the unit cell volume and therefore tolerance factors are a valid consideration for $NaNbO_3$ systems regardless of the A-site vacancy concentration.

Dense ceramics with relative density > 92 % were obtained for all compositions (see SI section 4 for more details). Backscattered electron images of polished and thermally etched samples for all compositions are shown in Figure 2 and SI section 4, Figure S9. For undoped $NaNbO_3$ a typical ceramic microstructure formed of equiaxial grains with a d_{50} of ~ 12.7 μm. For x = 0.05 grain size significantly increases to > 200 μm with a significant amount of pore entrapment which typically occurs when densification is lattice diffusion limited. For x = 0.10 and x = 0.15, a small amount of secondary phase is observed as bright regions. Point spectra energy dispersive X-ray (EDX) calculates a ~ 3:1 B:A-site ratio (SI section 4, Figure S11, S12 and Table S1, S2), corresponding to the phase $NaNb_3O_8$ according to the Na_2O-Nb_2O_5 phase diagram in Reference [32]. As the samples in this study were sintered at 1340 °C and $NaNb_3O_8$ has a eutectic at approximately 1280 °C it is proposed that this secondary phase forms a liquid phase during sintering resulting in excessive grain growth. For x = 0.05, any liquid phase may have re-dissolved into the lattice on cooling and is therefore undetectable by EDX (SI section 4, Figure S10). However it is worth noting that no secondary phases (other than TTB in x = 0.25) were observed by XRD in Figure 1 and therefore the formation of the secondary phases in the EDX data may be a result of the thermal etching process during sample preparation. It is also of note that $NaNb_3O_8$, which adopts a Wadsley-Roth type structure, is metastable according to the Na_2O – Nb_2O_5 phase diagram [32]; however, its clear presence observed by EDX at room temperature may demonstrate the potential improvement in thermodynamic stability of $NaNb_3O_8$ by Sr-doping.

The composition x = 0.20 shows evidence of core-shell behaviour with point EDX across the grain confirming core regions to be Sr-rich by ~ 1 at% compared to the darker shell region (SI section 4, Figure S13). For x = 0.25, EDX has confirmed the presence of secondary phase $Sr_2NaNb_5O_{15}$ as whole grains within the ceramic matrix as opposed to being a secondary phase located at the grain boundary or as intergrowths. Nevertheless, there is good agreement between the Sr and Na occupancies extracted from Rietveld refinements and the average at% calculated from EDX mapping for the perovskite phase and the nominal expected values across the complete compositional range (SI section 4, Figure S15). The systematic and lower than expected values for the Na at% content from EDX is associated with the challenges of obtaining quantitative data on a light element using this technique, as opposed significant levels of Na_2O loss due to volatilisation during sintering of ceramics.

Real permittivity (ε') and tan δ at 100 kHz against temperature and the temperature of maximum ε' (T_m) at 100 kHz against composition are shown in Figure 3(a) and (b), respectively. For undoped $NaNbO_3$, the RT permittivity and T_m are ~ 150 and ~ 369 °C which are consistent with literature [2, 11, 33]. An additional intermediate dielectric anomaly occurs

at ~ 150 °C which Qi et al. [11] have attributed to a subtle transition from a state of P→Q irreversibility to a region of P↔Q reversibility owing to the increase in thermodynamic degeneracy between the two polymorphs at higher temperature (SI section 5, Figure S16 for clearer evidence). For x = 0.05 the dielectric profile is retained however transitions occur at lower temperatures which may be due to the decrease in stabilisation of the antiferroelectric ordering and second-order Jahn-Teller effect which is responsible for the off-centering of Nb^{5+} ions within the oxygen octahedra as A-site vacancy concentration increases and the subsequent expansion of the unit cell and reduction in the pseudo-monoclinic tilting angle.

For x = 0.10 a significant change in the dielectric profile is observed, converting from the atypical P-phase profile into a single proper ferroelectric transition occurring at ~180 °C with little frequency dispersion (SI section 5, Figure S18). This is consistent with RT XRD findings where the P→Q polymorphic phase transition occurs at 0.05 < x < 0.10. Compositions x = 0.15 – 0.25 show relaxor-like behaviour at a lower temperature than the proper ferroelectric transition as evidenced by the degree of frequency dispersion (various frequencies plotted in Figure 3(a): ε' and tan δ against temperature at fixed frequencies for these compositions are shown in SI section 5, Figure S19 – S21). As shown in Figure 3(a), the broad relaxor-like dielectric behaviour observed at lower temperatures could be due to the chemical heterogeneity caused by this random distribution of A-site vacancies. Levin et al. [19] made similar observations based on the $Bi_xNa_{1-3x}NbO_3$ solid solution, where structural relaxations that occur to counteract the under-bonding of O^{2-} ions results in nanoscale modulations of the lattice distortions. In this study, the degree of chemical heterogeneity may then reduce at higher temperatures before undergoing a proper ferroelectric transition at approximately 120 °C for x = 0.15 and ~ 100 °C for x = 0.20 and 0.25.

Dielectric losses (tan δ) decrease initially with low levels of Sr^{2+} doping (i.e. ≤ 5 at%) and gradually increase for x > 0.05 as evidenced by the progressively lower temperature at which they exceed 0.05 (Figure 3 and SI section 5). For undoped $NaNbO_3$, the accelerated rate of increase in tan δ when compared to Sr-doped compositions may be due to the combination of electronic and ionic conduction which will be discussed in more detail later. The initial decrease in tan δ for $NaNbO_3$ from RT to ~ 100 °C is attributed to adsorption of water and is associated with proton conduction originating from the formation of oxygen vacancies [34] during synthesis and the subsequent transportation of H^+ through the bulk material or along the grain boundaries or outer surfaces of the ceramics.

As mentioned previously, local analysis of $Sr_xNa_{1-2x}NbO_3$ (x = 0.10, 0.15, 0.20) showed the systematic breaking of long-range order into polar Q-phase regions which is consistent with the findings of relaxor-like behaviour here. Although x = 0.15 – 0.25 could be successfully

indexed using only the $P2_1ma$ space group at room temperature, it is likely that these $P2_1ma$ clusters are distributed within a matrix of another crystallographic ordering, consistent with typical relaxor-ferroelectric behaviour where short-range polar regions are distributed in either a long-range polar or non-polar matrix. The $NaNbO_3$-$SrNb_2O_6$ phase diagram by Tang et al. [26] propose that $Sr_xNa_{1-2x}NbO_3$ with composition $0.15 < x < 0.22$ should show cubic symmetry. However, the arguments against the presence a cubic symmetry either as long-range translational symmetry or as a non-polar matrix are as follows: 1) *Pm*-3*m* $NaNbO_3$ shows no presence of in-phase or out-of-phase tilting reflections whereas in this study, there is clear evidence for both tilting components (A, B, and D in Figure 1(b)); 2) there is evidence in tan δ (Figure 3a) data of another phase transition occurring at ~ 250 °C (see SI section 5, Figures S18 – S21 for enhanced scale) for $x > 0.05$. It is logical to suggest that a transition at higher temperatures will be from a lower symmetry state to a higher symmetry state and is therefore only likely to show *Pm*-3*m* symmetry at temperatures > 250 °C; and 3) it is unreasonable to expect a predominantly cubic perovskite with non-displaced d^0 ions to exhibit polarisation to achieve the sufficiently high ε' values observed here. Combining these considerations with those of Torres-Pardo et al. [27, 28], it is likely that the increasing broadness of this relaxor-type behaviour for $x > 0.10$ is due to the decrease in coherence length of $P2_1ma$ polar clusters within in a polar matrix (either orthorhombic [*Pmnm* or *Cmcm*]) or tetragonal [*P*4/*mbm*] space group [35]) with reflections that are undetectable by conventional laboratory XRD, either due to the $P2_1ma$ reflection overlap or due to the weak/diffuse nature of the reflections not exceeding the detection limit of the equipment. As temperature increases from the temperature of maximum permittivity, the expansion of the unit cell (assuming positive thermal expansion) may assist in the long-range ordering of octahedral tilting, at which point the coherence length of polar clusters increases and more long-range symmetry is observed, before undergoing a proper ferroelectric-ferroelectric phase transition between ~ 80 and 120 °C depending on the Sr-content.

Polarisation – electric field (P-E) loops shown in Figure 4 may also provide evidence for this, as $x = 0.10$ to 0.25 both show clear signs of ferroelectric behaviour and maximum polarisation values comparable with typical polar ferroelectrics and relaxor ferroelectrics (values for maximum polarisation P_{max}, remnant polarisation P_r, coercive field E_C and energy storage properties given in SI section 6, Table S4). The presence of a polar matrix would explain the relatively high values for ε' observed at these compositions as the high domain wall density would be the basis of a significant polarisation required for ε' values >2000 whilst allowing for the possibility of transformations to higher symmetry states at higher temperatures. High resolution X-ray and/or neutron diffraction studies as a function of temperature would confirm/deny this hypothesis.

The increase in A-site vacancy concentration results in the almost linear decrease in the temperature of maximum permittivity (T_m) against composition at a rate of ~ -19 ^oC/at% as shown in Figure 3(b), which is consistent with the generation of ionic vacancies in other ferroelectric perovskites. Using $BaTiO_3$ as an example, isovalent doping of Ba^{2+} with Sr^{2+} results in a change in T_m of ~ -3 ^oC/at%, whereas aliovalent doping of Ba^{2+} by La^{3+} and the subsequent generation of B-site vacancies results in a change of ~ -24 ^oC/at% [36]. As the rate of decrease of T_m is consistent with that of vacancy generation in other ferroelectric perovskites, we believe the major solid solution of $NaNbO_3$-$SrNb_2O_6$ to be an A-site vacancy ionic compensation mechanism in air as opposed to the electronic donor doping compensation mechanism proposed by Klein et al. [37, 38]

The imaginary components of the impedance (-Z'') and electric modulus (M''/E_0) at ~ 600 ^oC against $\log_{10}$(frequency) are shown in Figure 5. Despite complexities in ceramic microstructure with regards to grain sizes, the formation of secondary phases, and core-shell behaviour in the case of x = 0.20, all compositions apparently show homogeneity in the electrical microstructure at elevated temperatures as evidenced by the agreement in relaxation frequencies (f_{max}) for the single Debye peaks in the combined Z'' and M''/E_0 spectra. To a first approximation, the IS data could be modelled on an equivalent circuit based on a single, parallel Resistor-Capacitor (RC) element. Capacitance values extracted from the M'' Debye maxima (based on the equation $C = 1/2M''_{max}$) correspond to between 53 $pF.cm^{-1}$ and 24 $pF.cm^{-1}$ and are therefore consistent with probing of the bulk (grain) response [39, 40]. For x = 0.20 the discrepancy in the ceramic microstructure and electrical microstructure may indicate that grains containing a core shell microstructure as observed by EDX mapping are not significantly contributing the bulk response and/or the difference in the relaxation frequencies of these regions are not significantly different at the elevated temperatures of > 350 ^oC where IS measurements were performed.

Arrhenius plots of bulk conductivity for all compositions are shown in Figure 6 and a simulated gradient corresponding to 1.4 eV has been plotted on the axes for comparison. None of the Arrhenius plots are linear over the measured temperature range and there is a change in E_a between ~ 500 and 600 ^oC for all compositions (SI section 7, Figure S22). In the high temperature (> 600 ^oC) region, bulk conductivity varies by approximately one order of magnitude and there is a trend of increasing conductivity for the Sr-doped compositions with x = 0.05 being the most insulating and x = 0.20 being the most conducting (Figure 6). x = 0.25 is beyond the solid solution limit and contains a secondary TTB phase but nevertheless the extracted bulk conductivity is in good agreement with x = 0.15 and 0.20. This indicates that the secondary phase is not contributing significantly to the IS response of the bulk response

for the main perovskite phase in this range. The E_a values for all Sr-doped samples in the high temperature range are between ~ 1.4 and 1.6 eV (SI section 7, Figure S23). The band gap of undoped $NaNbO_3$ is typically reported as being ~ 3.5 eV [41] which eliminates intrinsic electronic conduction across the band gap (E_{bg}) based on the assumption $E_a \sim E_{bg}/2$. Furthermore, the large change in Sr-content across the series is not altering E_a in this range in any systematic trend and is therefore unlikely to be associated with any lowering of E_{bg} with increasing Sr-content. The bulk conductivity of undoped $NaNbO_3$ lies in the middle of the range for the Sr-doped samples and has a significantly lower E_a value of ~ 1.1 eV, again eliminating intrinsic electronic conduction as the dominant mechanism in this temperature range.

Inspection of the low frequency response in the Z* plots of our ceramics (with Au electrodes) at 600 ^oC revealed evidence of a low frequency Warburg-type incline in the data for x = 0.00 but not for x > 0.00, Figure 7 (air response, inset). Although this indicates ionic conduction is present in our undoped $NaNbO_3$ ceramics, we are unable to identify it as Na^+ and/or O^{2-} ions and further studies are in progress. None of the Sr-doped samples showed evidence of a low frequency incline at low frequencies in the Z* plots. This does not eliminate the presence of ionic conduction in these samples in this range as they may be mixed ionic-electronic conductors.

To investigate for n or p-type electronic conductivity in our ceramics IS measurements were conducted in flowing N_2 at 600 ^oC to lower the oxygen partial pressure, pO_2 and to compare the results to that obtained in air. For undoped $NaNbO_3$, there was a modest decrease in the total resistivity on switching from air to N_2 from ~ 185 to 160 kΩcm based on the low frequency intercept on the Z' axis in the Z* plot, Fig 7 (a). This indicates modest n-type conduction is present in these ceramics. In contrast, f_{max} of the M'' peak associated with the bulk response was invariant with pO_2, Figure 8 (a) suggesting the bulk conductivity is not influenced by this modest change in pO_2 at 600 ^oC. The weak n-type dependence of the total resistivity of the ceramics based on the Z* plots therefore indicates there must be an additional electroactive region in these ceramics and this is attributed to a small (n-type) grain boundary contribution. Based on the results presented, it is not possible to fully establish the electrical properties of our undoped $NaNbO_3$ ceramics but we propose they contain mixed ionic-electronic behaviour and further studies are in progress to test this hypothesis.

The pO_2 dependent behaviour of the Sr-doped compositions displayed a clear and systematic trend of increasing n-type behaviour with increasing x based on both the Z* plots (total resistivity) and M'' spectra (bulk conductivity). In the case of Z* plots, the total resistivity decreased in the lower pO_2 by a factor ~ 5, 6 and 8 for x = 0.05, 0.10 and 0.15-0.25, respectively, Fig 7 (b) – (f). In the case of M'' spectra, f_{max} of the M'' peak increases in the

lower pO_2, Figure 8 (b) – (f). The ratio can be estimated as ~ 6 for x = 0.05 and 0.10 as f_{max} of the M'' peak is below the upper frequency limit of the instrumentation. The data for x = 0.15 - 0.25 are shown to illustrate the trend observed from M'' spectra is consistent across all samples. It is noteworthy that the total resistivity based on the Z* responses for x = 0.15 and 0.20 in both atmospheres are very similar with values of ~ 20 and 2.5 kΩcm in air and N_2, respectively. x = 0.25 displays the same trend but the magnitudes of the total resistivity are larger with values of ~ 34 and 4 kΩcm in air and N_2, respectively. These larger values may be attributed to the geometric factor correction to the data which assumes the volume fraction of sample to be exclusively perovskite whereas this sample contains a significant level of TTB as a secondary phase.

It is clear from the Arrhenius plot of bulk conductivity in Figure 6 and the Z* plots and M'' spectra in Figures 7 and 8 that the increase in A-site vacancy concentration with Sr doping has a significant effect of the reducibility of the material. We propose that as the A-site vacancy concentration increases, so too does the concentration of under-bonded O^{2-} ions within the lattice. This then allows for, at high temperature and/or low pO_2, the increasing tendency for O^{2-} ions to leave the lattice which is then compensated by partial reduction of Nb^{5+} to Nb^{4+} ions as shown in Equation (1) and (2):

$$O_O^X \rightarrow \frac{1}{2}O_{2(g)} + V_O^{\bullet\bullet} + 2e' \quad (1)$$

$$2e' + 2Nb_{Nb}^X \rightarrow 2Nb'_{Nb} \quad (2)$$

This defect mechanism therefore dominates the electronic component of the bulk conduction properties of $Sr_xNa_{1-2x}NbO_3$ ceramics for x ≥ 0.05 over the range of ~ 600 °C in air and flowing N_2. At this stage we cannot comment on any ionic contribution (Na^+ or O^{2-}) to the bulk conductivity for x ≥ 0.05 and further studies are in progress to establish the level (if any) of mixed conductivity.

4. Conclusions

The crystallographic, microstructural, dielectric, and ferroelectric properties of $Sr_xNa_{1-2x}NbO_3$ (x = 0.00, 0.05, 0.10, 0.15, 0.20, 0.25) have been investigated by means of X-ray diffraction (XRD), scanning electron microscopy (SEM), dielectric spectroscopy (DS) and impedance spectroscopy (IS). XRD shows an almost linear expansion of the unit cell with compositions which stabilises the ferroelectric Q-phase at x ≥ 0.10 and is retained until the solid solution limit at 0.20 < x < 0.25. SEM shows the potential for liquid phase sintering and subsequently

a significant increase in the grain size for x = 0.05, 0.10, and 0.15 with the potential formation of $NaNb_3O_8$ with a eutectic 60 ^oC lower than the sintering temperature used in this study. DS shows a gradual decrease in the temperature of maximum permittivity (T_m) of ~ -19 ^oC/at%, consistent with values expected for ionic vacancy generation. Arrhenius plots of conductivity show ~ 1 order of magnitude increase in conductivity for $x \geq 0.05$ and temperatures > 600 ^oC which can be attributed to the increasing tendency for under bonded O^{2-} ions to leave the lattice at high temperature and subsequently partially reduce Nb^{5+} to Nb^{4+} ions as shown by the Z* plots and M'' spectra at varying pO_2 levels.

Acknowledgements

The authors would like to thank the Engineering and Physical Sciences Research Council (EPSRC) for financial support (New directions in high temperature dielectrics: unlocking performance of doped tungsten bronze oxides through mechanistic understanding, EP/V05337X/1) and Professor Andrew J Bell (University of Leeds) for use of the Radiant Precision LC Analyser.

Author Contributions

Thomas E. Hooper: Data curation, Formal analysis, Writing – original draft, review & editing

Derek C. Sinclair: Conceptualisation, Supervision, Writing – original draft, review & editing

References

[1] N. Hadaeghi, M. Dai, Y. Zhang, R. Xie, H. Nouri & H. Zhang, Origin of antiferroelectricity in $NaNbO_3$. *Physical Review Materials* **2024,** *8*, 015004 10.1103/PhysRevMaterials.8.015004

[2] M.-H. Zhang, L. Fulanović, C. Zhao & J. Koruza, Review on field-induced phase transitions in lead-free $NaNbO_3$-based antiferroelectric perovskite oxides for energy storage. *Journal of Materiomics* **2023,** *9* (1), 1-18 10.1016/j.jmat.2022.09.008

[3] P. Zhao, L. Li & X. Wang, $BaTiO_3$-$NaNbO_3$ energy storage ceramics with an ultrafast charge-discharge rate and temperature-stable power density. *Microstructures* **2023**, 10.20517/microstructures.2022.21

[4] G. Li, Z. Yi, Y. Bai, W. Zhang & H. Zhang, Anisotropy in photocatalytic oxidisation activity of $NaNbO_3$ photocatalyst. *Dalton Transactions* **2012,** *41*, 10194 doi.org/10.1039/C2DT30593C

[5] X. Li, G. Li, S. Wu, X. Chen & W. Zhang, Preparation and photocatalytic properties of platelike $NaNbO_3$ based photocatalysts. *Journal of Physics and Chemistry of Solids* **2014,** *75*, 491-494 10.1016/j.jpcs.2013.12.008

[6] J. Koruza, H. Liu, M. Höfling, M.-H. Zhang & P. Veber, (K,Na)NbO_3-based piezoelectric single crystals: Growth methods, properties, and applications. *Journal of Materials Research* **2020,** *35* (8), 990-1016 10.1557/jmr.2019.391

[7] J.-F. Li, K. Wang, F.-Y. Zhu, L.-Q. Cheng & F.-Z. Yao, (K,Na)NbO_3-Based Lead-free piezoceramics-Fundamental aspects, processing techniques, and remaining challenges. *Journal of the American Ceramic Society* **2013,** *96* (12), 3677-3696 10.1111/jace.12715

[8] Y. I. Yuzyuk, P. Simon, E. Gagarina, L. Hennet, D. Thiaudière, V. I. Torgashev, S. I. Raevskaya, I. P. Raevskii, L. A. Reznitchenko & J. L. Sauvajol, Modulated phases in $NaNbO_3$: Raman scattering, synchrotron x-ray diffraction, and dielectric investigations. *Journal of Physics: Condensed Matter* **2005,** *17* (33), 4977-4990 10.1088/0953-8984/17/33/003

[9] I. Lefkowitz, K. Łukaszewicz & H. D. Megaw, The high-temperature phases of sodium niobate and the nature of transitions in pseudosymmetric structures. *Acta Crystallographica* **1966,** *20* (5), 670-683 10.1107/s0365110x66001592

[10] Y. Fan, Z. Zhou, R. Liang, M. Zhou & X. Dong, The effect of A-site nonstoichiometry on the microstructure, electric properties, and phase stability of $NaNbO_3$ polycrystalline ceramics. *Journal of the European Ceramic Society* **2019,** *39* (15), 4712-4718 10.1016/j.jeurceramsoc.2019.06.041

[11] H. Qi, G. Wang, Y. Zhang, D. Wang, H. Liu, S. Deng, R. Zuo & J. Chen, Tunable phase structure in NaNbO3 ceramics by grain-size effect, electric field and heat treatment. *Acta Materialia* **2023,** *248*, 10.1016/j.actamat.2023.118778

[12] J. M. Rosso, J. A. Burato, V. F. Freitas, D. M. Silva, E. A. Volnistem, G. M. Santos, T. G. M. Bonadio, G. S. Dias, L. F. Cotica & I. A. Santos, Evidence of the stable existence of a morphotropic phase boundary in the $BaTiO_3$-$NaNbO_3$ system. *Materials Chemistry and Physics* **2019,** *237*, 121794

[13] S. K. Sarkar & M. L. Sharma, Dielectric strength and dielectric constant of $BaTiO_3$-$NaNbO_3$ composites at room temperature. *Journal of Materials Science Letters* **1989,** *8*, 1365-1367 10.1007/BF00720188

[14] S. Xie, K. Zhu, J. Qiu & H. Guo, Microstructure and electrical properties of $NaNbO_3$-$BaTiO_3$ lead-free piezoelectric ceramics. *Frontiers of Mechanical Engineering in China* **2009,** *4* (3), 345-349 10.1007/s11465-009-0050-9

[15] A. Prasatkhetragarn, R. Saenarpa, B. Yotburut, P. Ketsuwan, T. Sareein, S. Ananta & R. Yimnirum, Investgations on morphology and ferroelectric properties of $NaNbO_3$-$PbTiO_3$ composite ceramics. *Ferroelectrics* **2011,** *416* (1), 40-46 10.1080/00150193.2011.577664

[16] S. Dash, R. Padhee, P. R. Das & R. N. P. Choudhary, Enhancement of dielectric and electrical properties of $NaNbO_3$-modified $BiFeO_3$. *Journal of Materials Science: Materials in Electronics* **2013,** *24*, 3315-3323 10.1007/s10854-013-1249-4

[17] M. De, S. Hajra, R. Tiwari, S. Sahoo, R. N. P. Choudhary & H. S. Tewari, Structural, dielectric and electrical characteristic of $BiFeO_3$-$NaNbO_3$ solid solutions. *Ceramics International* **2018,** *44*, 11792-11797 10.1016/j.ceramint.2018.03.263

[18] X. Lei, Z. Peng, P. Liang, D. Wu, X. Chao & Z. Yang, Realizing oxygen ion conduction in perovskite structure $NaNbO_3$ by A-site Bismuth doping. *Journal of Alloys and Compounds* **2022,** *924*, 10.1016/j.jallcom.2022.166506

[19] I. Levin, F. Yang, R. Maier, W. J. Laws, D. S. Keeble, G. Cibin & D. C. Sinclair, Displacive Order–Disorder Behavior and Intrinsic Clustering of Lattice Distortions in Bi-Substituted $NaNbO_3$. *Advanced Functional Materials* **2020,** *30* (30), 10.1002/adfm.202001840

[20] S. Aso, H. Matsuo & Y. Noguchi, Reversible electric-field-induced phase transition in Ca-modified $NaNbO_3$ perovskites for energy storage applications. *Scientific Reports* **2023,** *13* (1), 6771 10.1038/s41598-023-33975-6

[21] B. Liu & X. Tan, Structure, ferroelectric, and dielectric properties of $(Na_{1-2x}Ca_x)NbO_3$ ceramics. *Journal of Materials Research* **2021,** *36* (5), 1076-1085 10.1557/s43578-020-00020-5

[22] A. P. Pivovarova, V. I. Strakhov & V. P. Popov, Phase relations in the $LaNb_3O_9$ - $NaNbO_3$ system in the temperature range of 20 to 800 °C. *Refractories and Industrial Ceramics* **2001,** *42*, 7-8 10.1023/A:1012718529213

[23] D. O. Mishchuk, O. I. V'yunov, O. V. Ovchar & A. G. Belous, Structural and dielectric properties of solid solutions of sodium niobate in lanthanum and neodymium niobates. *Inorganic Materials* **2004,** *40* (12), 1324-1330 10.1007/s10789-005-0019-y

[24] A. P. Pivovarova & V. I. Strakhov, High-temperature electrical conductivity of solid solutions in the system $NaNbO_3$-$NdNb_3O_9$. *Refractories and Industrial Ceramics* **1999,** *40* (7-8), 307-308 10.1007/BF02762575

[25] M. L. López, I. Álvarez-Serrano, A. Galdámez, E. Rodríguez-Aguado, E. Rodríguez-Castellón & Y. Saad, New dielectric anomalies in the A-site highly deficient $NaxNbO_3$ electroceramics. *Ceramics International* **2020,** *46* (10), 16770-16780 10.1016/j.ceramint.2020.03.253

[26] D.-S. Tang, J.-K. Liang, T.-J. Shi, Y.-L. Zhang, J.-H. Tian & W.-H. Li, Investigation of the pseudo ternary system $SrNb_2O_6$-$NaNbO_3$-$LiNbO_3$. *Acta Physica Sinica* **1979,** *28* (1), 62-77 10.7498/aps.28.62

[27] A. Torres-Pardo, R. Jiminez, J. M. Gonzalez-Calbet & E. Garcia-Gonzalez, Room temperature ferroelectric in $Na_{1-x}Sr_{x/2}\square_{x/2}NbO_3$ through the introduction of cationic vacancies. *Chemistry of Materials* **2008,** *20*, 6957-6964 10.1021/cm802101r

[28] A. Torres-Pardo, R. Jiminez, J. M. Gonzalez-Calbet & E. Garcia-Gonzalez, Induction of relaxor behaviour in $Na_{1-x}Sr_{x/2}\square_{x/2}NbO_3$ through the introduction of cationic vacancies. *Chemistry of Materials* **2009,** *21*, 2193-2200 10.1021/CM9000834

[29] G. Gouget, F. Mauvy, U.-C. Chung, S. Fourcade, M. Duttine, M.-D. Braida, T. Le Mercier & A. Demourges, Associating and tuning sodium and oxygen mixed-ion conduction in niobium-based perovskites. *Advanced Functional Materials* **2020,** *30*, 1909254 10.1002/adfm.201909254

[30] B. H. Toby & R. B. Von Dreele, GSAS-II: the genesis of a modern open-source all purpose crystallography software package. *Journal of Applied Crystallography* **2013,** *46* (2), 544-549 10.1107/s0021889813003531

[31] R. D. Shannon, Revised Effective Ionic Radii and Systematic Studies of Interatomic Distances in Halides and Chalcogenides. *Acta Crystallographica* **1976,** *A32*, 751-767 10.1107/S0567739476001551

[32] A. Popovič, L. Bencze, J. Koruza, B. Malič & M. Kosec, Knudsen effusion mass spectrometric approach to the thermodynamics of Na_2O–Nb_2O_5 system. *International Journal of Mass Spectrometry* **2012,** *309*, 70-78 10.1016/j.ijms.2011.08.028

[33] K. Konieczny, Pyroelectric and dielectric study of $NaNbO_3$ single crystals. *Materials Science and Engineering* **1999,** *B60*, 124-127 10.1016/S0921-5107(99)00004-5

[34] Y. Meng, J. Gao, Z. Zhao, J. Amoroso, J. Tong & K. S. Brinkman, Review: recent progress in low-temperature proton-conducting ceramics. *Journal of Materials Science* **2019,** *54* (13), 9291-9312 10.1007/s10853-019-03559-9

[35] C. N. Darlington & K. S. Knight, High-temperature phases of $NaNbO_3$ and $NaTaO_3$. *Acta Crystallographica Section B* **1999,** *55* (1), 24-30 10.1107/s010876819800963x

[36] F. D. Morrison, D. C. Sinclair & A. R. West, Doping mechanisms and electrical properties of La-doped BaTiO3 ceramics. *International Journal of Inorganic Materials* **2001,** *3*, 1205-1210 10.1016/S1466-6049(01)00128-3

[37] N. Bein, B. Kmet, T. Rojac, A. B. Golob, B. Malič, J. Moxter, T. Schneider, L. Fulanovic, M. Azadeh, T. Frömling, et al., Fermi energy, electrical conductivity, and the energy gap of $NaNbO_3$. *Physical Review Materials* **2022,** *6* (8), 084404 10.1103/PhysRevMaterials.6.084404

[38] A. Klein, K. Albe, N. Bein, O. Clemens, K. A. Creutz, P. Erhart, M. Frericks, E. Ghorbani, J. P. Hofmann, B. Huang, et al., The Fermi energy as common parameter to describe charge compensation mechanisms: A path to Fermi level engineering of oxide electroceramics. *Journal of Electroceramics* **2023,** *51* (3), 147-177 10.1007/s10832-023-00324-y

[39] J. T. S. Irvine, D. C. Sinclair & A. R. West, Electroceramics: Characterization by Impedance Spectroscopy. *Advanced Materials* **2004,** *2* (3), 132-138 10.1002/adma.19900020304

[40] A. R. West, D. C. Sinclair & N. Hirose, Characterization of Electrical Materials, Especially Ferroelectrics, by Impedance spectroscopy. *Journal of Electroceramics* **1997,** *1* (1), 65-71 10.1023/A:1009950415758

[41] G. Gouget, M. Duttine, E. Durand, A. Villesuzanne, V. Rodriguez, F. Adamietz, T. Le Mercier, M.-D. Braida & A. Demourgues, Isolating the Two Room-Temperature Polymorphs of $NaNbO_3$: Structural Features, Optical Band Gap, and Reactivity. *ACS Applied Electronic Materials* **2019,** *1* (4), 513-522 10.1021/acsaelm.8b00125

Figures, Tables and Captions

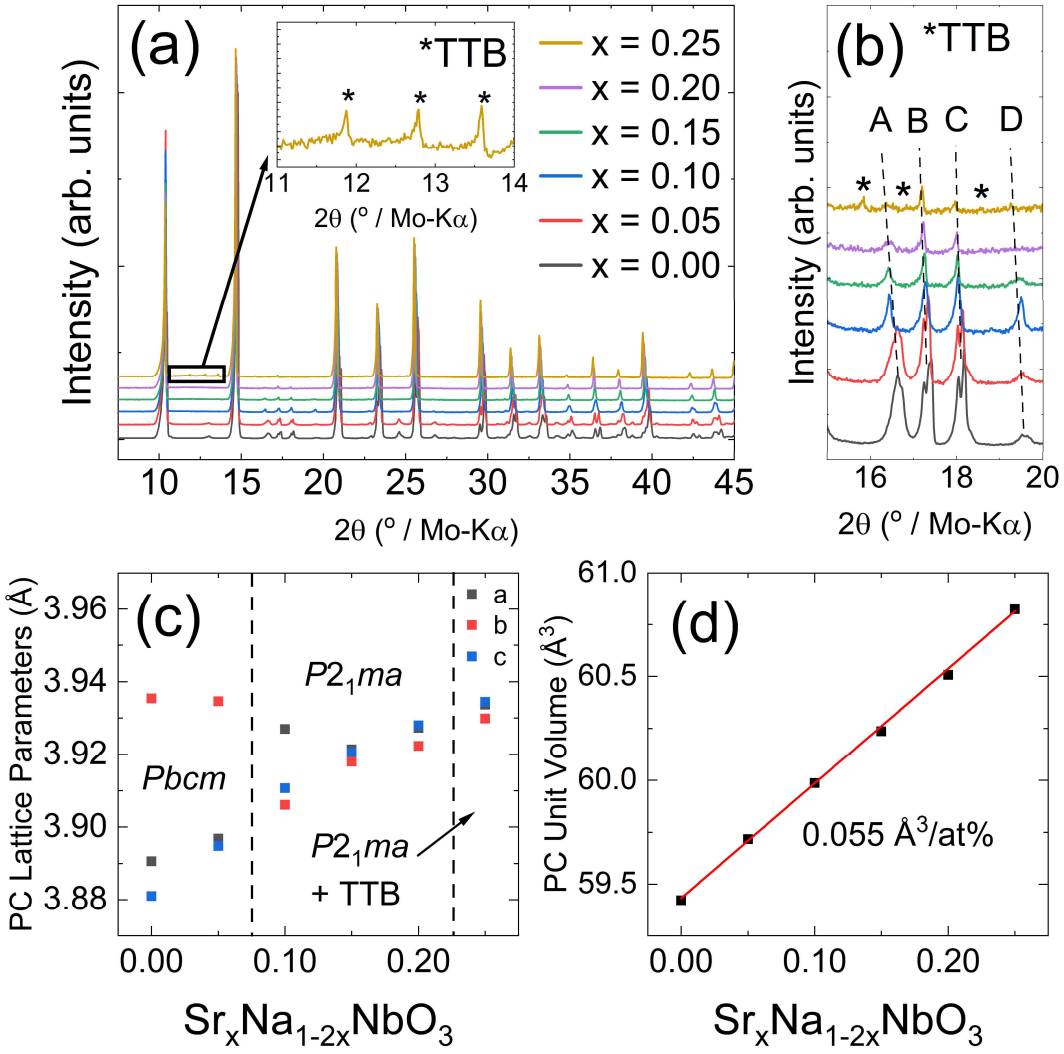

Figure 1: (a) Stacked XRD plots from 8° – 45° 2θ for crushed and annealed $Sr_xNa_{1-2x}NbO_3$ (x = 0.00, 0.05, 0.10, 0.15, 0.20, and 0.25) samples. Inset shows the magnified plot of $Sr_{0.25}Na_{0.50}NbO_3$ from 11° – 14° 2θ to demonstrate the presence of tetragonal tungsten bronze (TTB) secondary phase and solid solution limit. Rietveld refinements for all compositions can be found in Supplementary Information Figures S7. (b) Magnified stacked XRD plots for all compositions from 15° – 20° 2θ. Reflections A and D are associated with in-phase tilting whereas reflection B is caused by out-of-phase rotations and reflection C is the pseudo cubic (111) for a perovskite lattice. (c) Pseudo cubic (PC) lattice parameters against composition. Dashed lines represent approximate compositional locations of the polymorphic phase transition from antiferroelectric *Pbcm* (P) phase to ferroelectric $P2_1ma$ (Q) to Q + TTB secondary phase. (d) Pseudo cubic (PC) unit cell volume against composition. Error bars in (c) and (d) are hidden by symbol size.

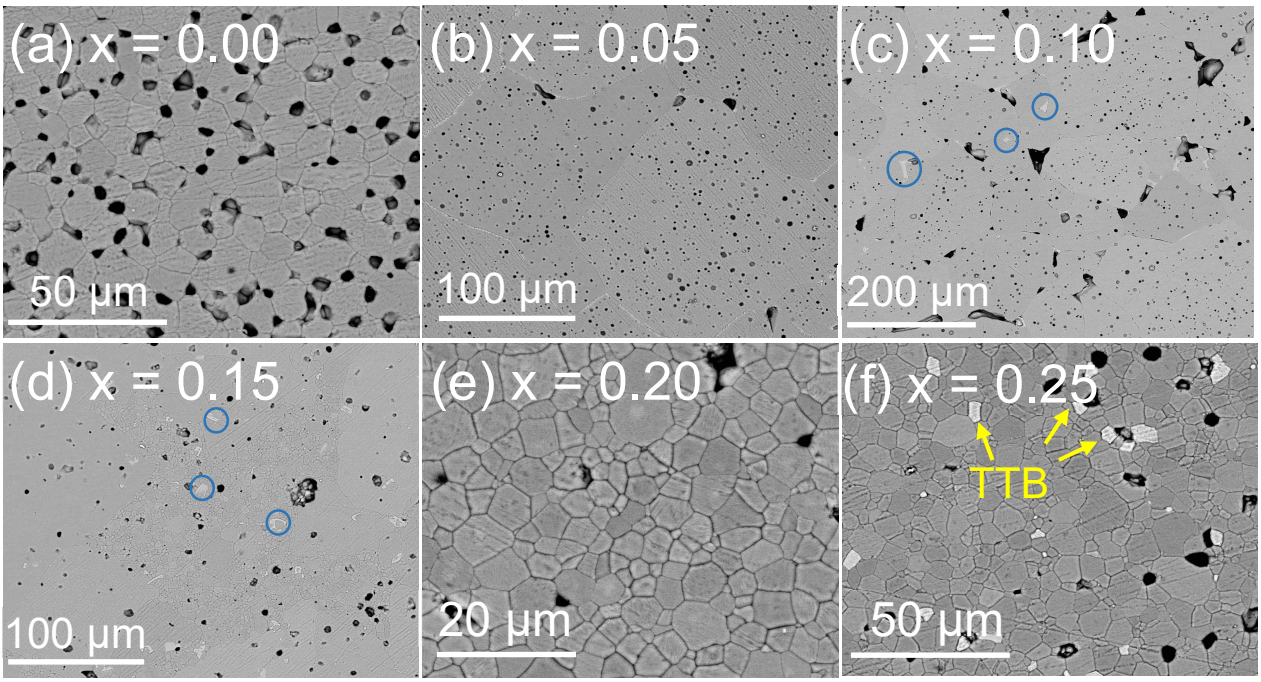

Figure 2: Backscattered electron images of polished and thermally etched $Sr_xNa_{1-2x}NbO_3$ bulk ceramics where x = (a) 0.00, (b) 0.05, (c) 0.10, (d) 0.15, (e) 0.20, and (f) 0.25. Blue circles in x = 0.10 and x = 0.15 highlight regions of $NaNb_3O_8$ identified via point EDX spectra (SI section 4, Figure S11, S12 and Table S1, S2). Yellow arrows are used in x = 0.25 to highlight tetragonal tungsten bronze (TTB) secondary phase identified by point EDX spectra (SI section 4, Figure S14 and Table S3)

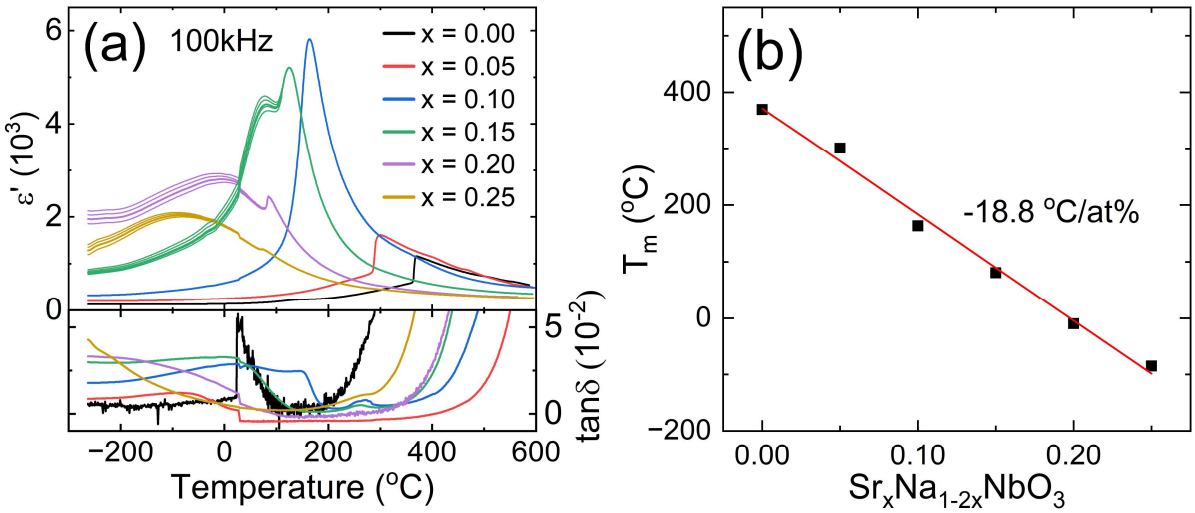

Figure 3: (a) Real permittivity (ε') and tan δ at 100 kHz against temperature for all compositions. 1, 10, 250, and 1000 kHz data has been presented in the dielectric spectroscopy plots for x = 0.15, 0.20, and 0.25 to demonstrate frequency dispersion in the relaxor-like dielectric anomaly. Discontinuities at ~ 25 °C are where high and low temperature dielectric data has been stitched together. (b) Temperature of maximum permittivity (T_m) against composition.

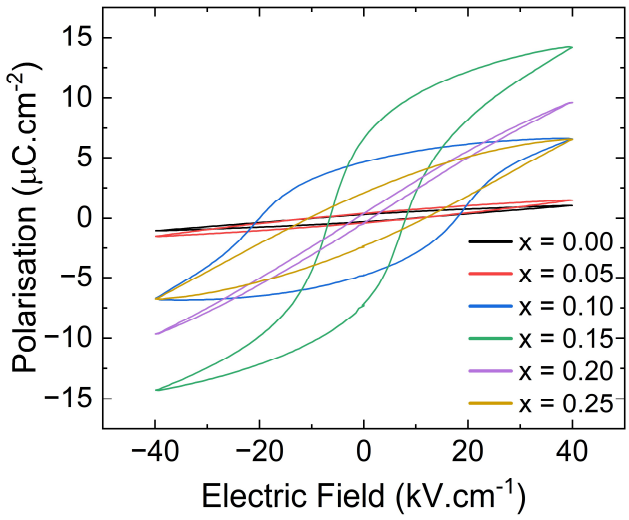

Figure 4: Room temperature polarisation against electric field up to ±40 kV.cm^{-1} for all compositions.

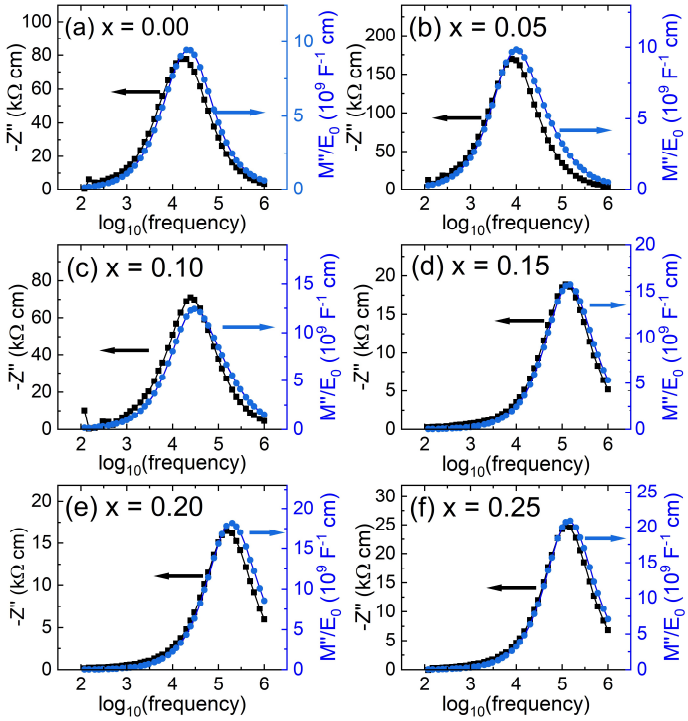

Figure 5: Imaginary components of impedance (Z'') and electric modulus (M''/E_0) at ~ 600 °C versus $\log_{10}$(frequency) for (a) x = 0.00, (b) x = 0.05, (c) x = 0.10, (d) x = 0.15, (e) x = 0.20, and (f) x = 0.25.

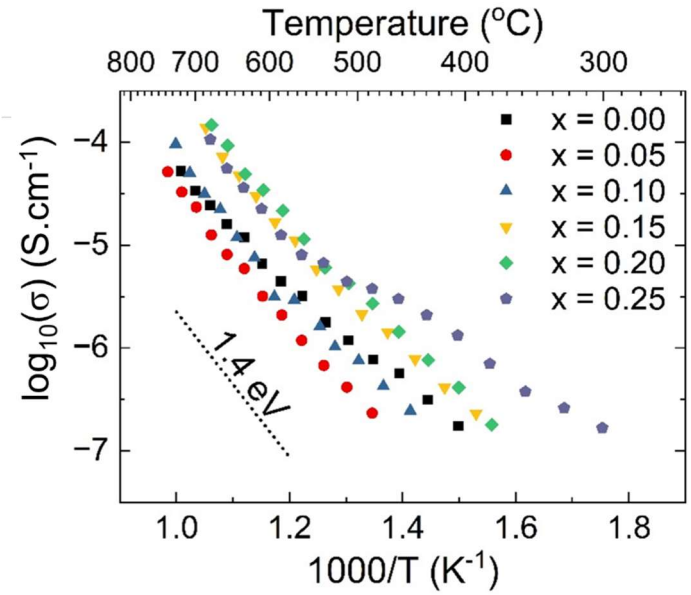

Figure 6: Arrhenius plots of conductivity for all compositions. A simulated activation energy of 1.4 eV has been added for comparison to experimental data.

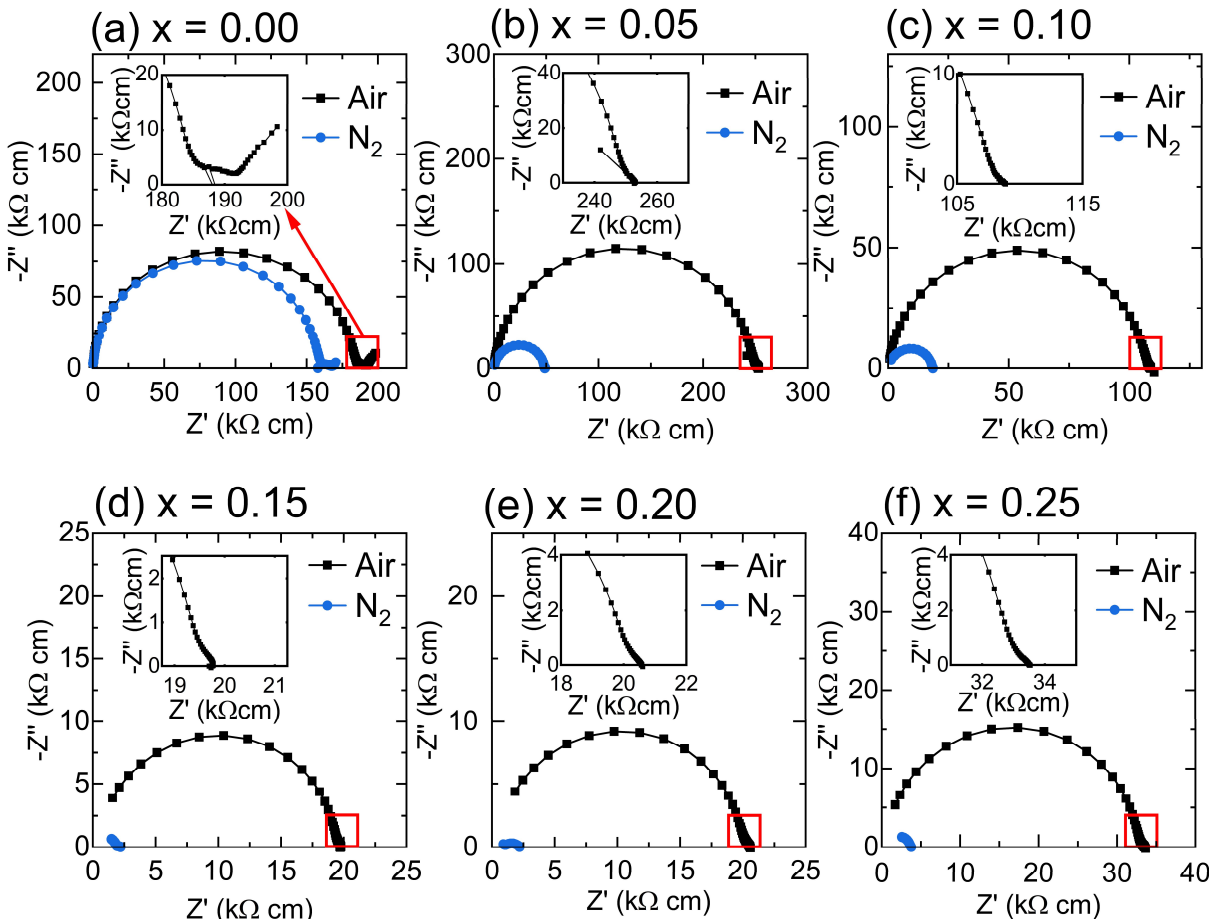

Figure 7: Complex impedance plots (-Z'' vs. Z') for (a) x = 0.00, (b) x = 0.05, (c) x = 0.10, (d) x = 0.15, (e) x = 0.20, and (f) x = 0.25 at ~ 600 °C in air and after being left overnight in flowing N_2. Inset shows a zoomed in complex impedance plots for the response in air at the x-intercepts as highlighted by red boxes.

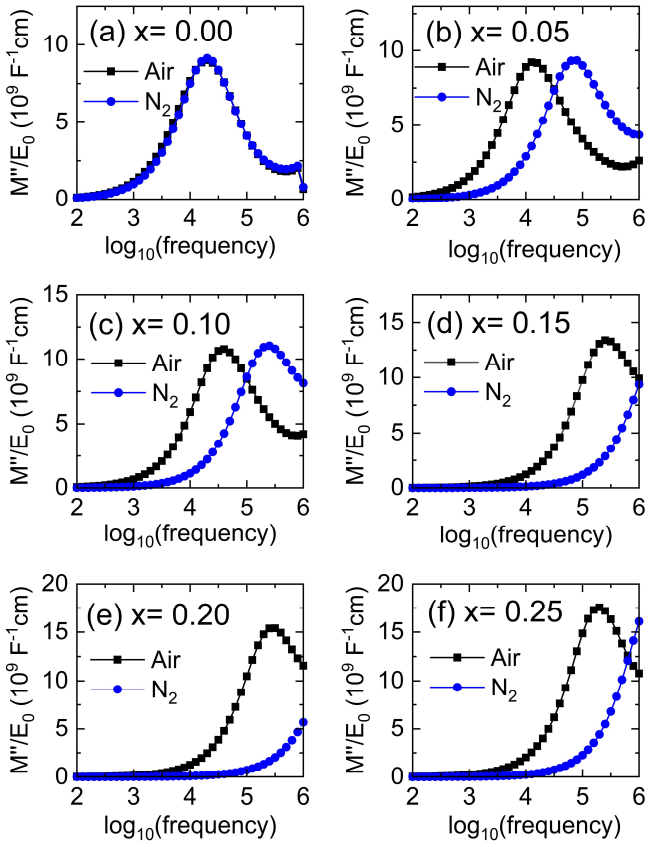

Figure 8: Electric modulus (M''/E_0) versus $\log_{10}$(frequency) in air and flowing N_2 at 600 °C for (a) x = 0.00, (b) x = 0.05, (c) x = 0.10, (d) x = 0.15, (e) x = 0.20, and (f) x = 0.25. The upturn in M'' data at high frequencies after the M'' peaks in (a) – (c) is an artefact associated with the measuring jig as opposed to a sample-related response.

Table 1: Orthorhombic (*Pbcm* for x = 0.00 & x = 0.05; $P2_1ma$ for x = 0.10, 0.15, 0.20, and 0.25) lattice parameters, cell volume, geometric and theoretical density values, and fitting parameters gathered from Rietveld refinements (all refinements available in SI section 3, Figure S6)

$Sr_xNa_{1-2x}NbO_3$	a (Å)	b (Å)	c (Å)	Volume ($Å^3$)	$\rho_{geometric}$ ($g.cm^{-3}$) [%]	$\rho_{theoretical}$ ($g.cm^{-3}$)	R_P (%)	R_{wp} (%)	χ^2
0	5.5021(9)	5.5655(9)	15.5241(2)	475.37(11)	4.24 [92.6]	4.58	2.55	7.37	8.38
0.05	5.5109(7)	5.5644(7)	15.5792(2)	477.73(9)	4.48 [97.7]	4.59	1.90	4.77	6.33
0.1	5.5536(1)	7.8122(1)	5.5305(1)	239.95(1)	4.53 [98.3]	4.61	1.69	4.38	6.70
0.15	5.5457(4)	7.8360(4)	5.5446(5)	240.95(3)	4.61 [98.0]	4.71	1.70	4.50	7.00
0.20	5.5540(7)	7.8447(1)	5.5550(7)	242.03(4)	4.64 [98.4]	4.71	1.30	2.840	4.77
0.25	5.5631(4)	7.8597(2)	5.5642(3)	243.29(2)	4.64 [97.4]	4.76	1.23	2.53	4.28

Structural, Dielectric, and Conduction Behaviour of A-site deficient $Sr_xNa_{1-2x}NbO_3$ Ceramics

Thomas E. Hooper[1] and Derek C. Sinclair

Department of Materials Science and Engineering, Sir Robert Hadfield Building, University of Sheffield, Mappin Street, Sheffield S1 3JD, UK

Supplementary Information

Contents

[1] Corresponding author: thomas.elliot.hooper@gmail.com

List of Figures

Figure S12: Backscattered electron micrograph of polished and thermally etched $Sr_{0.15}Na_{0.70}NbO_3$ bulk ceramic, annotated with point spectra positions.

Figure S13: Point spectra across a grain in polished and thermally etched $Sr_{0.20}Na_{0.60}NbO_3$ and corresponding atomic percentage to demonstrate core-shell microstructure.

Figure S14: Backscattered electron micrograph of polished and thermally etched $Sr_{0.25}Na_{0.50}NbO_3$ bulk ceramic, annotated with point spectra positions.

Figure S15: Sr^{2+} and Na^{+} occupancies extracted from Rietveld refinements (solid data points) and average at% calculated from EDX mapping (hollow data points) against composition. Dashed lines correspond to nominal $Sr_xNa_{1-2x}NbO_3$

Figure S16: (a) Real component of permittivity (ε') and (b) tan δ at fixed frequencies against temperature for $NaNbO_3$ (x = 0.00)

Figure S17: (a) Real component of permittivity (ε') and (b) tan δ at fixed frequencies against temperature for $Sr_{0.05}Na_{0.90}NbO_3$ (x = 0.05). Sub-zero tan δ are due to electrical noise (inductance) from electrical testing equipment.

Figure S18: (a) Real component of permittivity (ε') and (b) tan δ at fixed frequencies against temperature for $Sr_{0.10}Na_{0.80}NbO_3$ (x = 0.10)

Figure S19: (a) Real component of permittivity (ε') and (b) tan δ at fixed frequencies against temperature for $Sr_{0.15}Na_{0.70}NbO_3$ (x = 0.15)

Figure S20: (a) Real component of permittivity (ε') and (b) tan δ at fixed frequencies against temperature for $Sr_{0.20}Na_{0.60}NbO_3$ (x = 0.20)

Figure S21: (a) Real component of permittivity (ε') and (b) tan δ at fixed frequencies against temperature for $Sr_{0.25}Na_{0.50}NbO_3$ (x = 0.25)

Figure S22: Arrhenius plots of conductivity calculated using M'' peak height at the relaxation frequency for (a) $NaNbO_3$, (b) $Sr_{0.05}Na_{0.90}NbO_3$, (c) $Sr_{0.10}Na_{0.80}NbO_3$, (d) $Sr_{0.15}Na_{0.70}NbO_3$, (e) $Sr_{0.20}Na_{0.60}NbO_3$, and (f) $Sr_{0.25}Na_{0.50}NbO_3$.

Figure S23: High temperature and low temperature activation energies extrapolated from Arrhenius plots of conductivity against composition.

List of Tables

SI Section S1: Analysis of Reagents

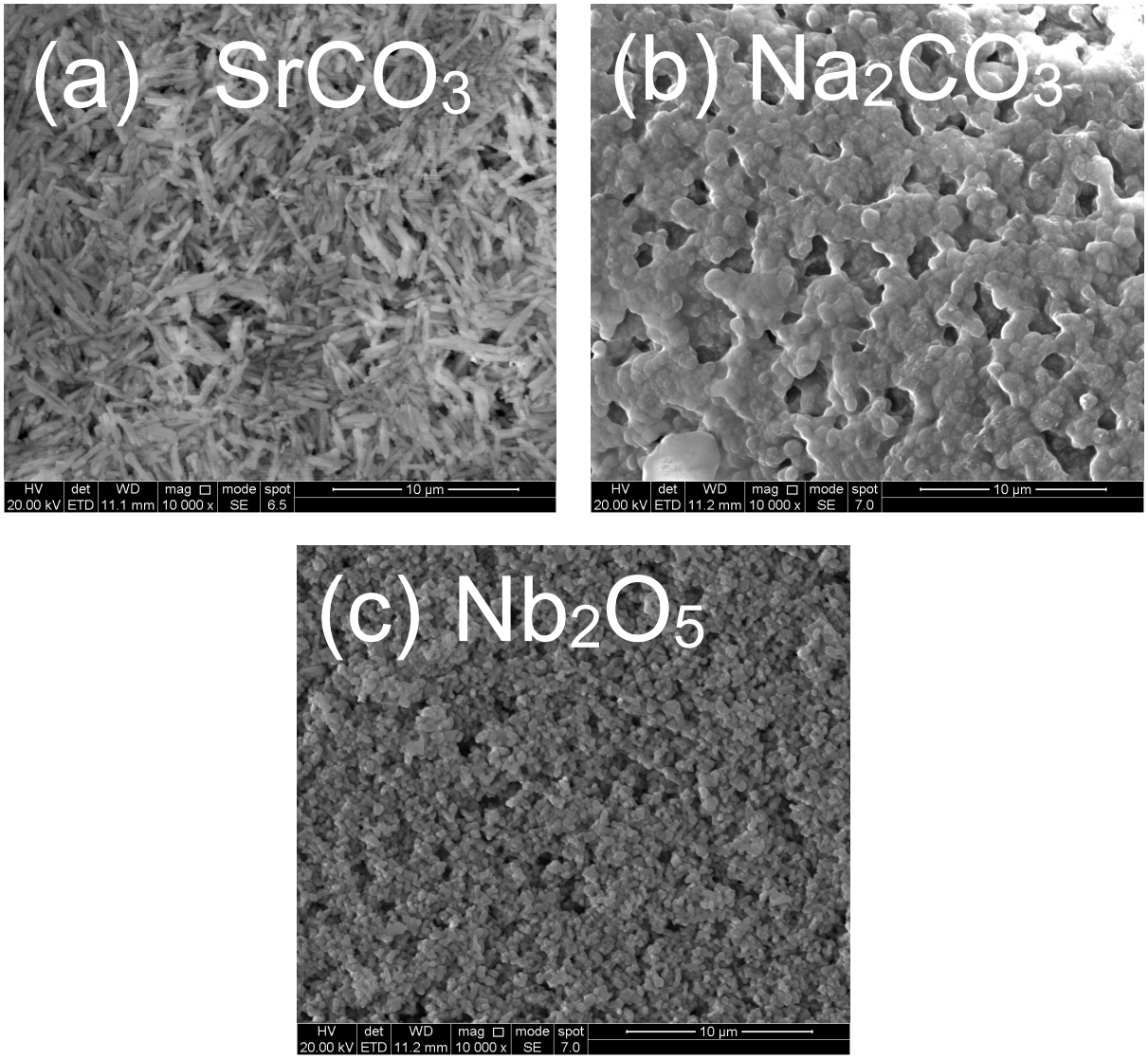

Figure S1: Secondary electron images of reagents (a) $SrCO_3$, (b) Na_2CO_3, and (c) Nb_2O_5 after dehydration.

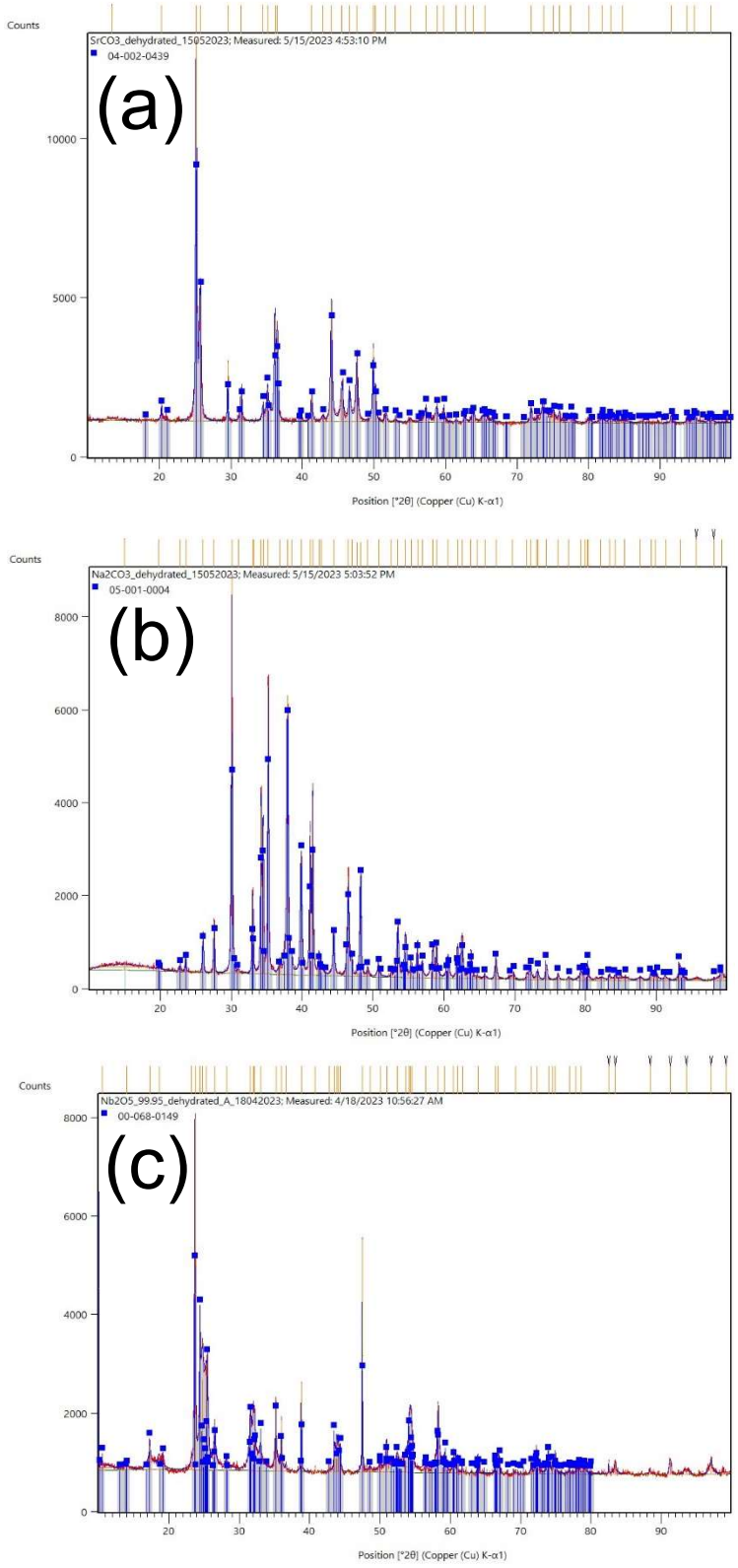

Figure S2: Stacked X-ray diffraction patterns from 10-100° 2θ (Cu-Kα source) of (a) $SrCO_3$ (fully indexed to orthorhombic *Pnma*), (b) Na_2CO_3 (fully indexed to orthorhombic *Pca*2_1), and (c) Nb_2O_5 (fully indexed to orthorhombic *C*2/*c*) reagents after dehydration.

SI Section S2: Analysis of calcined powders

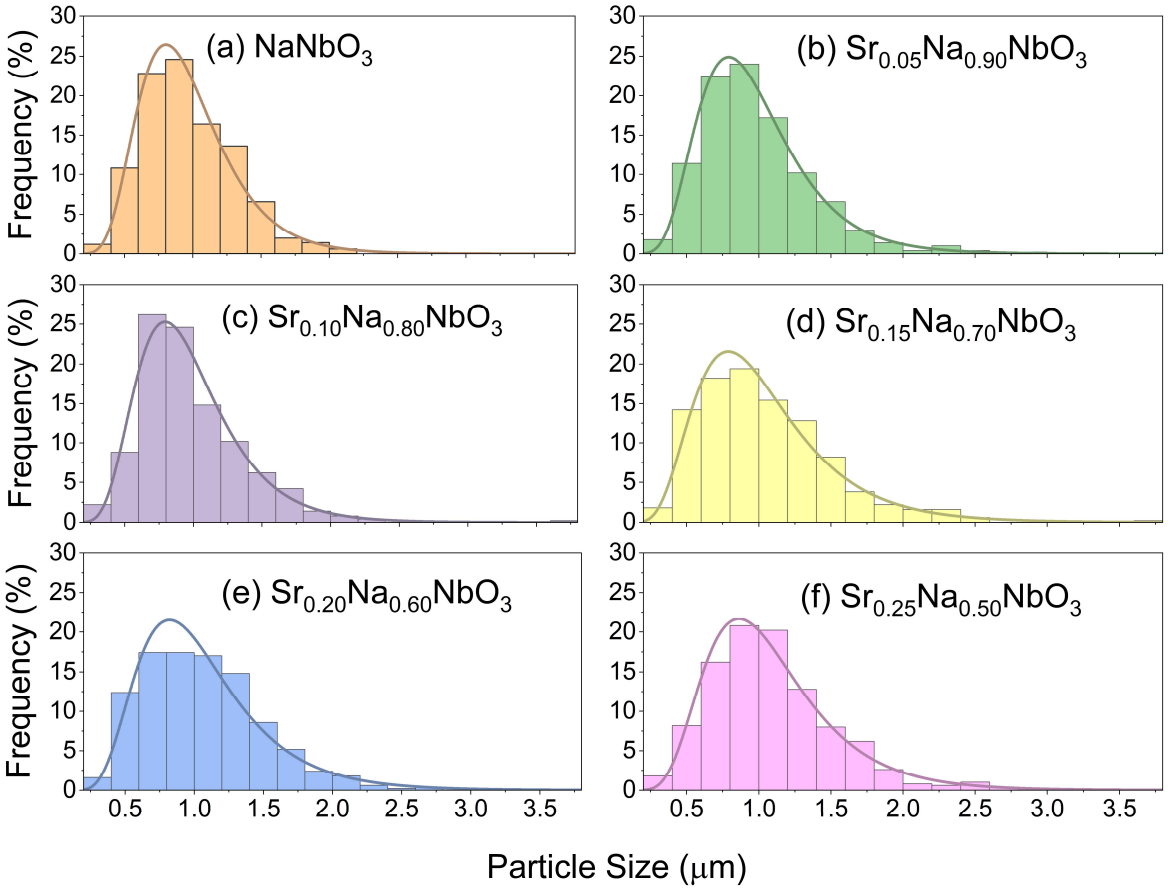

Figure S3: Particle size distributions of powders used for pressing for (a) $NaNbO_3$ (x = 0.00), (b) $Sr_{0.05}Na_{0.90}NbO_3$ (x = 0.05), (c) $Sr_{0.10}Na_{0.80}NbO_3$ (x = 0.10), (d) $Sr_{0.15}Na_{0.70}NbO_3$ (x = 0.15), (e) $Sr_{0.20}Na_{0.6}NbO_3$ (x = 0.20), and (f) $Sr_{0.25}Na_{0.50}NbO_3$ (x = 0.25). 500 particles across 3 secondary electron micrographs were measured.

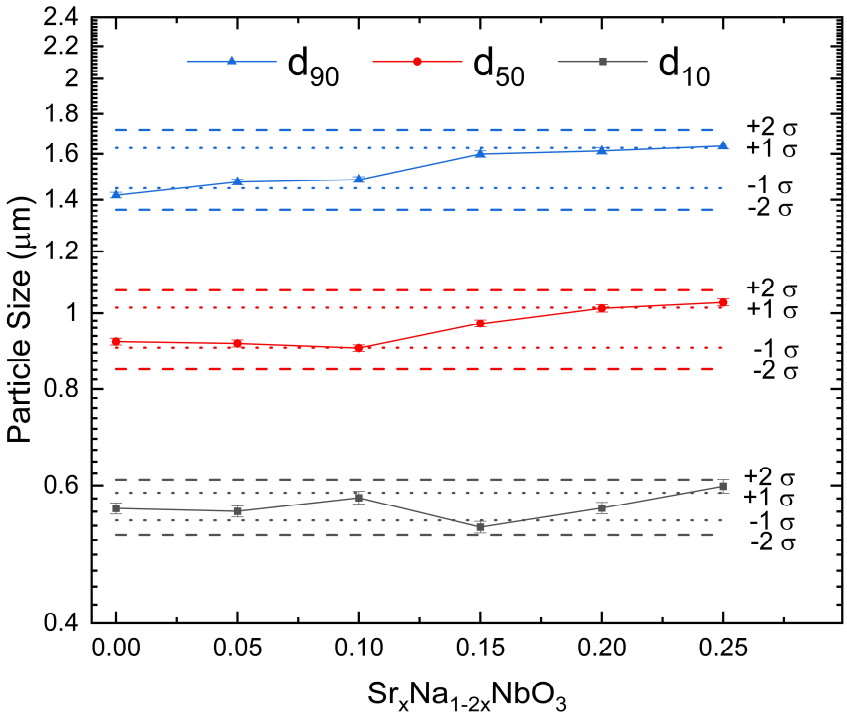

Figure S4: Average d_{10}, d_{50}, and d_{90} against composition for powders used for pressing. Dotted and dashed lines represent ± 1 and ± 2 standard deviations (σ), respectively.

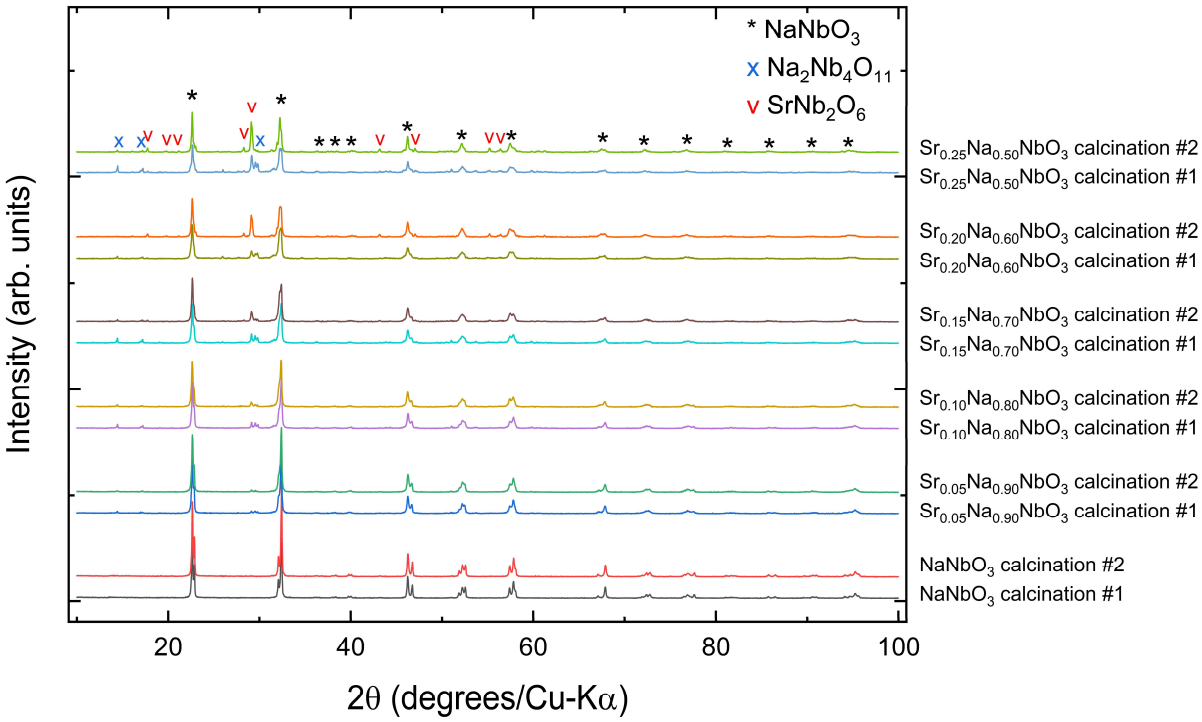

Figure S5: XRD patterns from 10-100° 2θ and step size 0.02° for calcined powders after first and second calcination for all compositions.

SI Section S3: X-ray diffraction and Rietveld Refinements

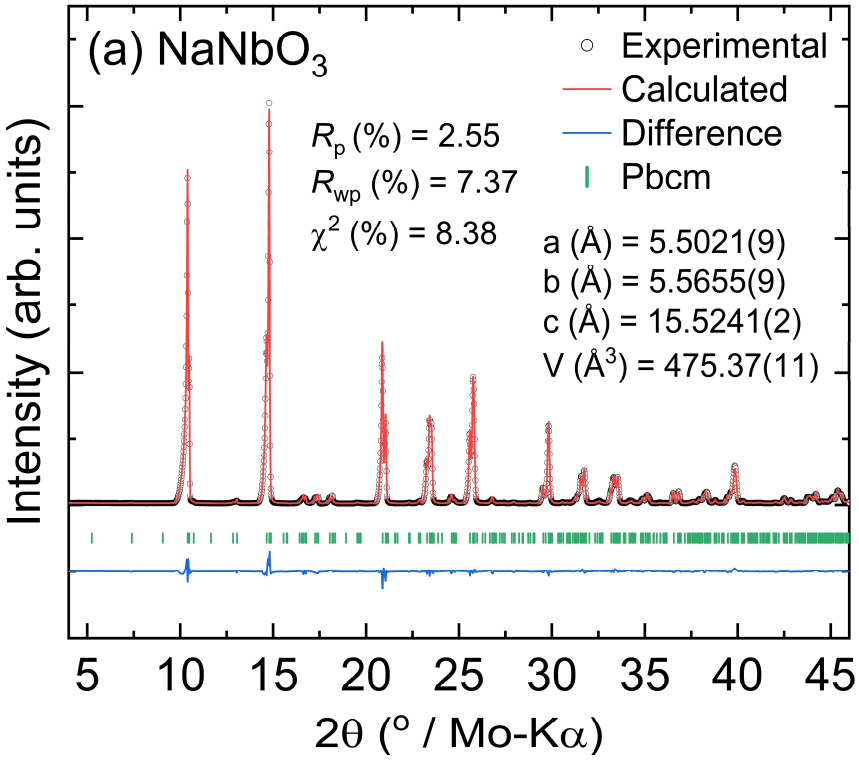

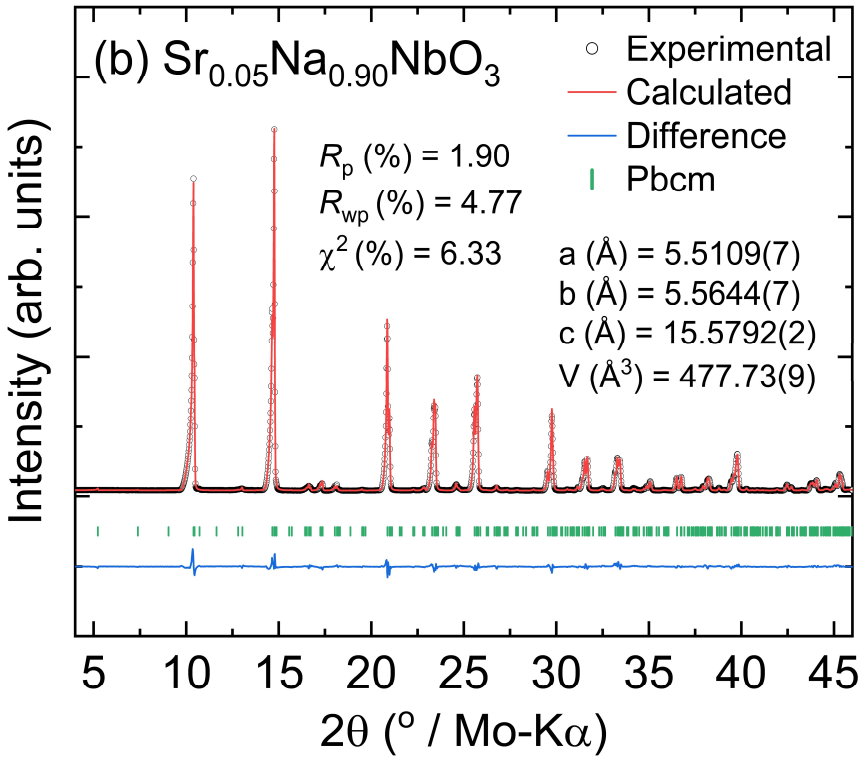

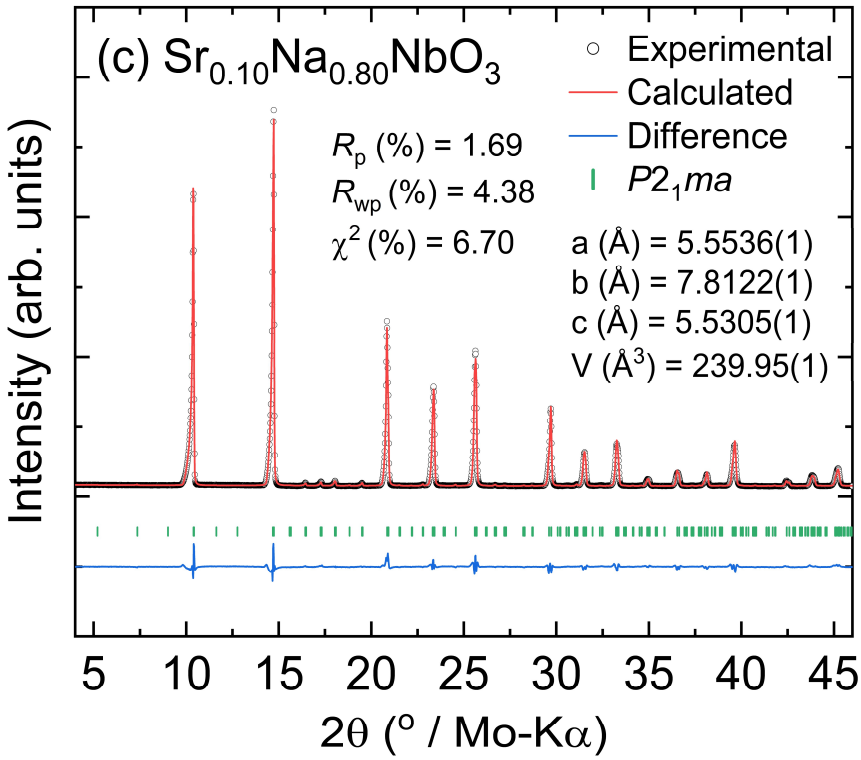
(c) Sr0.10Na0.80NbO3
Experimental
Calculated
Difference
P21ma
Rp (%) = 1.69
Rwp (%) = 4.38
χ2 (%) = 6.70
a (Å) = 5.5536(1)
b (Å) = 7.8122(1)
c (Å) = 5.5305(1)
V (Å3) = 239.95(1)
Intensity (arb. units)
5 10 15 20 25 30 35 40 45
2θ (° / Mo-Kα)

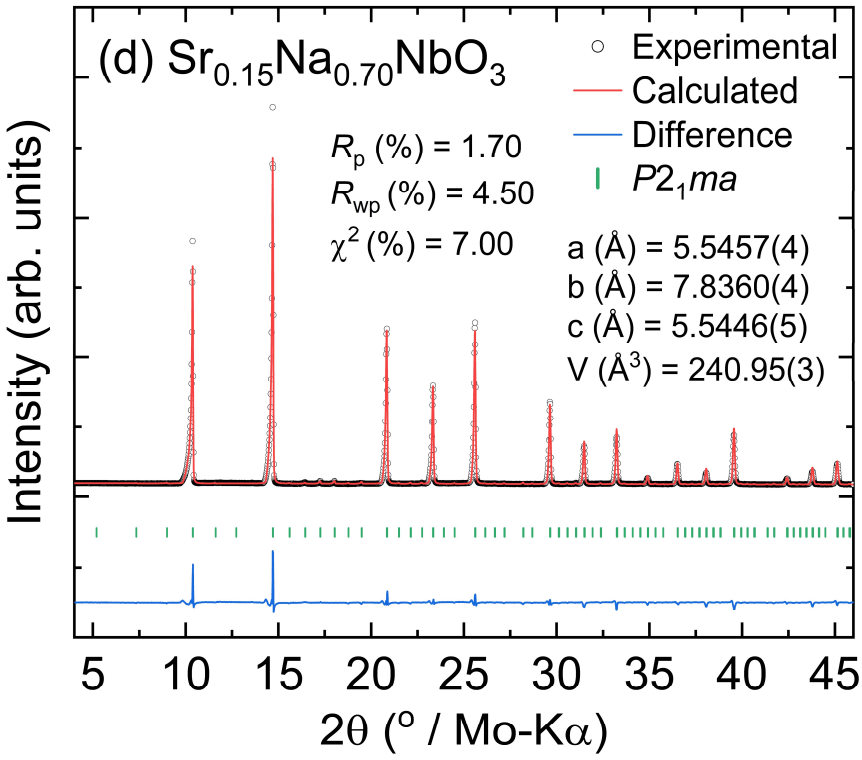
(d) Sr0.15Na0.70NbO3
Experimental
Calculated
Difference
P21ma
Rp (%) = 1.70
Rwp (%) = 4.50
χ2 (%) = 7.00
a (Å) = 5.5457(4)
b (Å) = 7.8360(4)
c (Å) = 5.5446(5)
V (Å3) = 240.95(3)
Intensity (arb. units)
5 10 15 20 25 30 35 40 45
2θ (° / Mo-Kα)

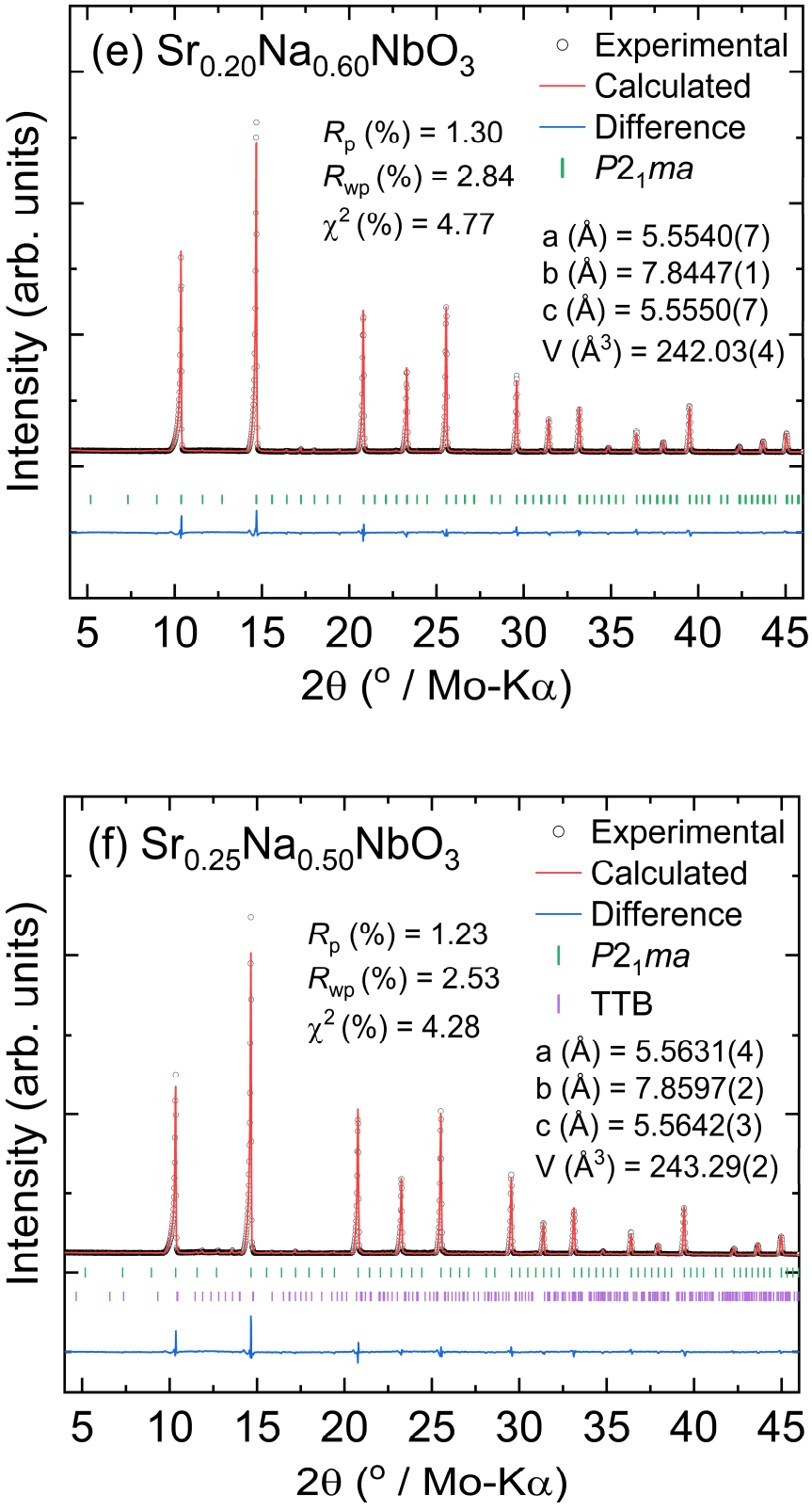

Figure S6: Rietveld refinements for (a) $NaNbO_3$, (b) $Sr_{0.05}Na_{0.90}NbO_3$, (c) $Sr_{0.10}Na_{0.80}NbO_3$, (d) $Sr_{0.15}Na_{0.70}NbO_3$, (e) $Sr_{0.20}Na_{0.60}NbO_3$, and (f) $Sr_{0.25}Na_{0.50}NbO_3$

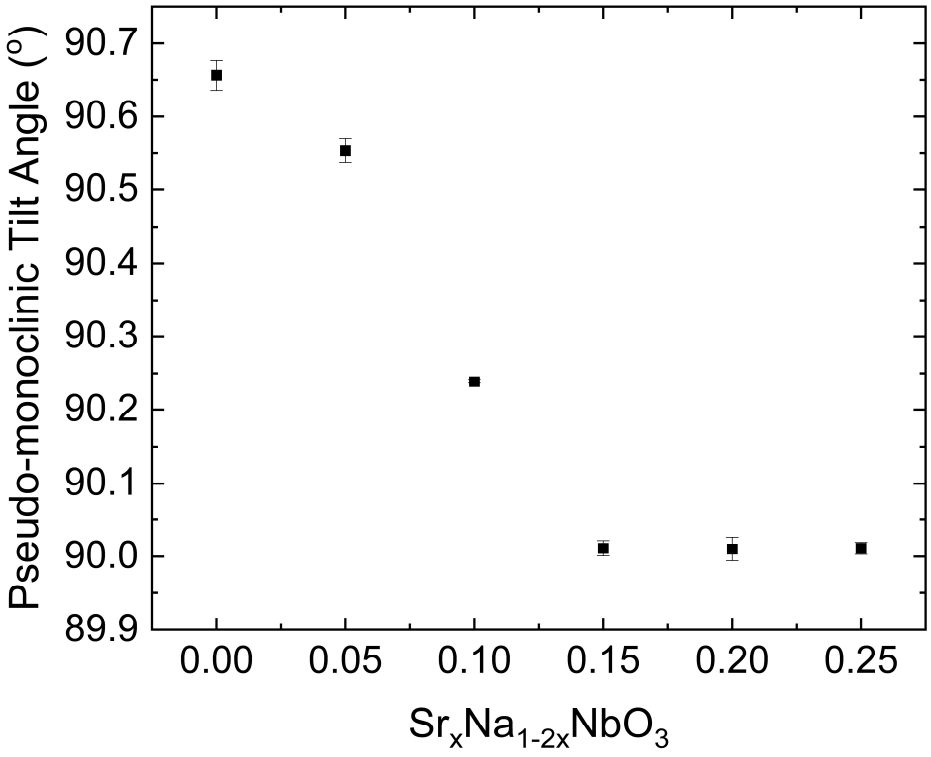

Figure S7: Pseudo-monoclinic tilt angle ($2\tan^{-1}(c_O/b_O)$, where c_O and b_O represent the orthorhombic lattice parameters) against composition.

SI Section S4: Microstructural Analysis

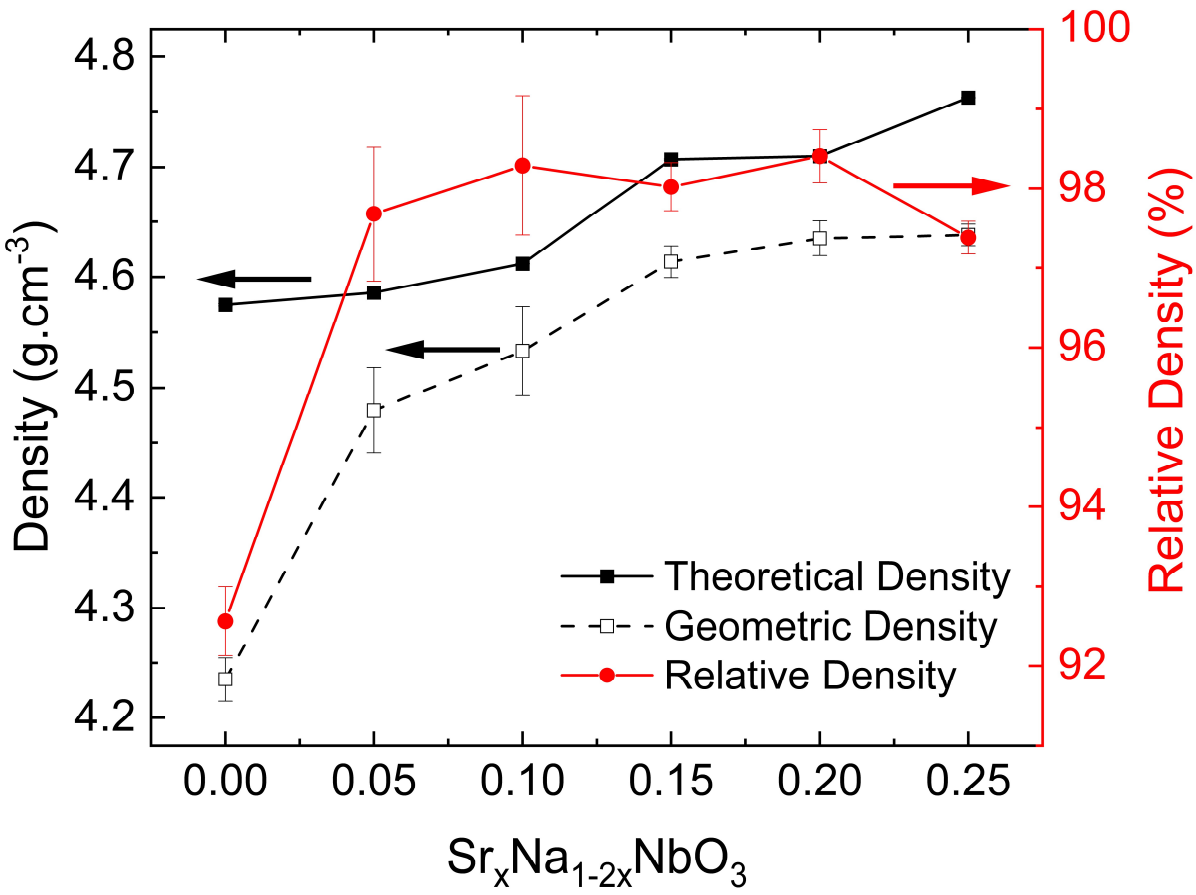

Figure S8: Geometric density, theoretical density calculated using lattice parameters from XRD refinements, and relative density against composition. Error bars correspond to standard error from the measurements of 5 samples.

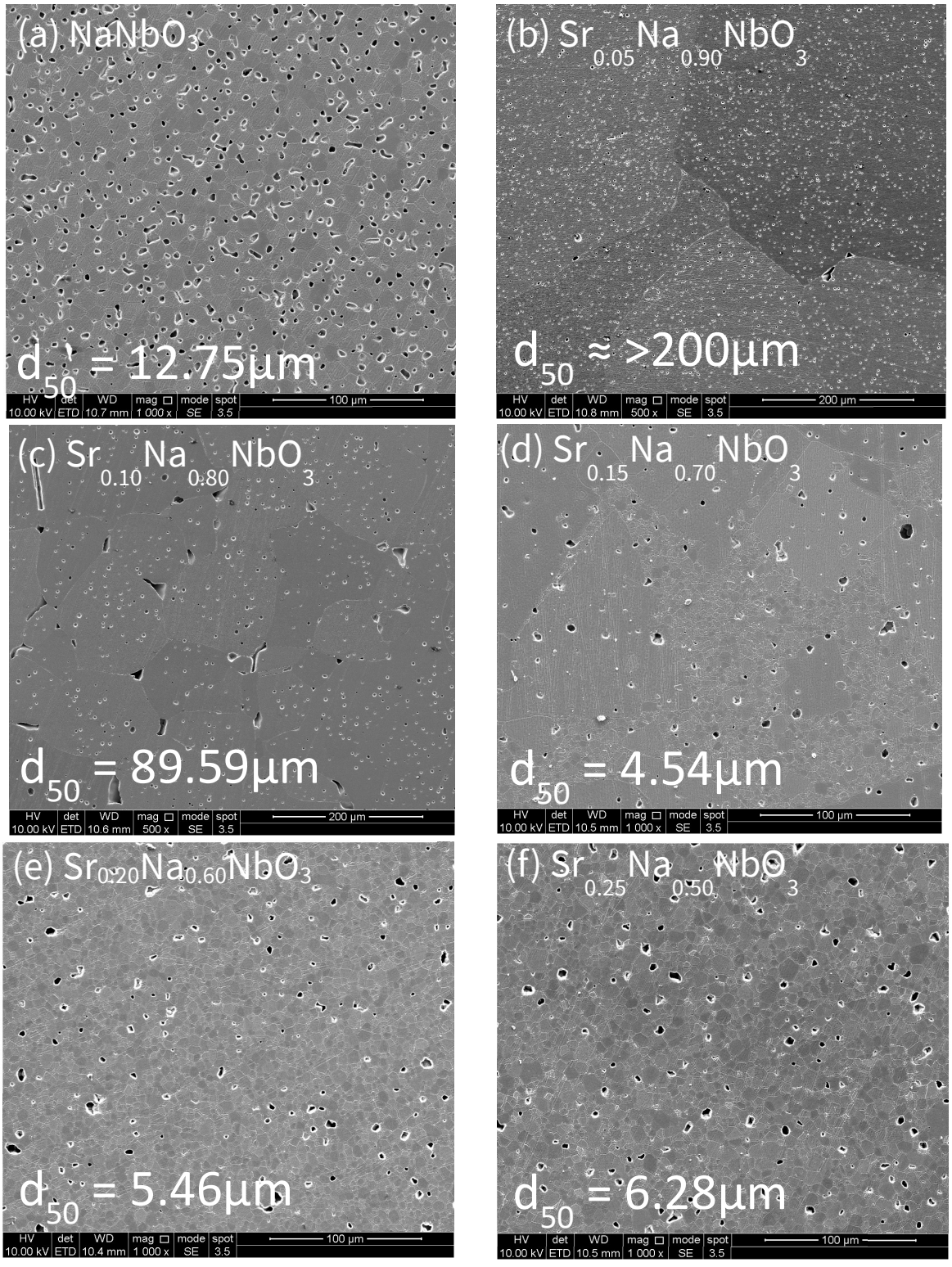

Figure S9: Secondary electron micrographs of polished and thermally etched samples for compositions (a) $NaNbO_3$, (b) $Sr_{0.05}Na_{0.90}NbO_3$, (c) $Sr_{0.10}Na_{0.80}NbO_3$, (d) $Sr_{0.15}Na_{0.70}NbO_3$, (e) $Sr_{0.20}Na_{0.60}NbO_3$, and (f) $Sr_{0.25}Na_{0.50}NbO_3$. Particle size determined by measuring 200 individual particles across 3 secondary electron micrographs using ImageJ software.

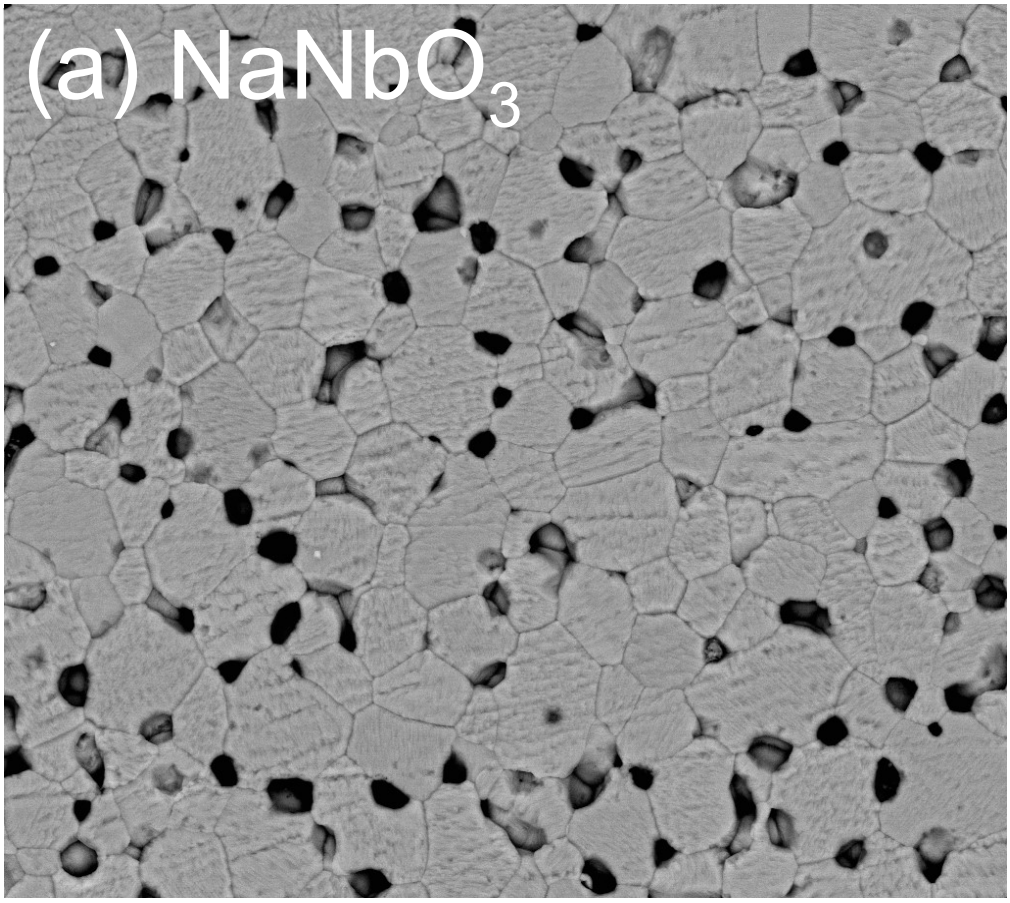
(a) NaNbO3
25μm

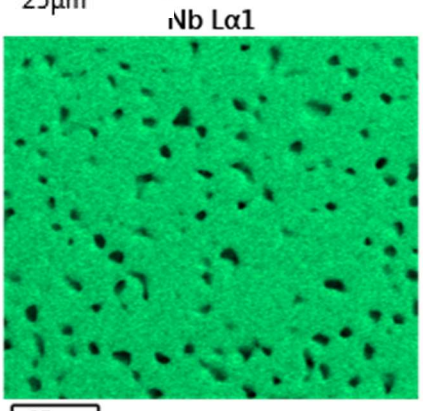
Nb Lα1
25μm

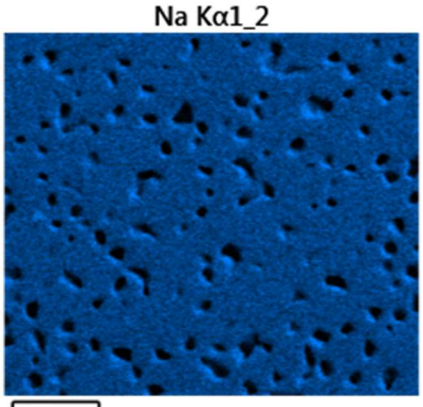
Na Kα1_2
25μm

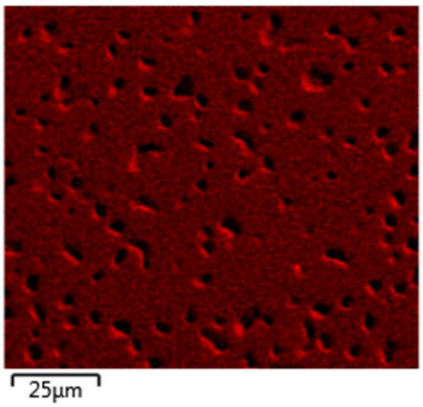
O Kα1
25μm

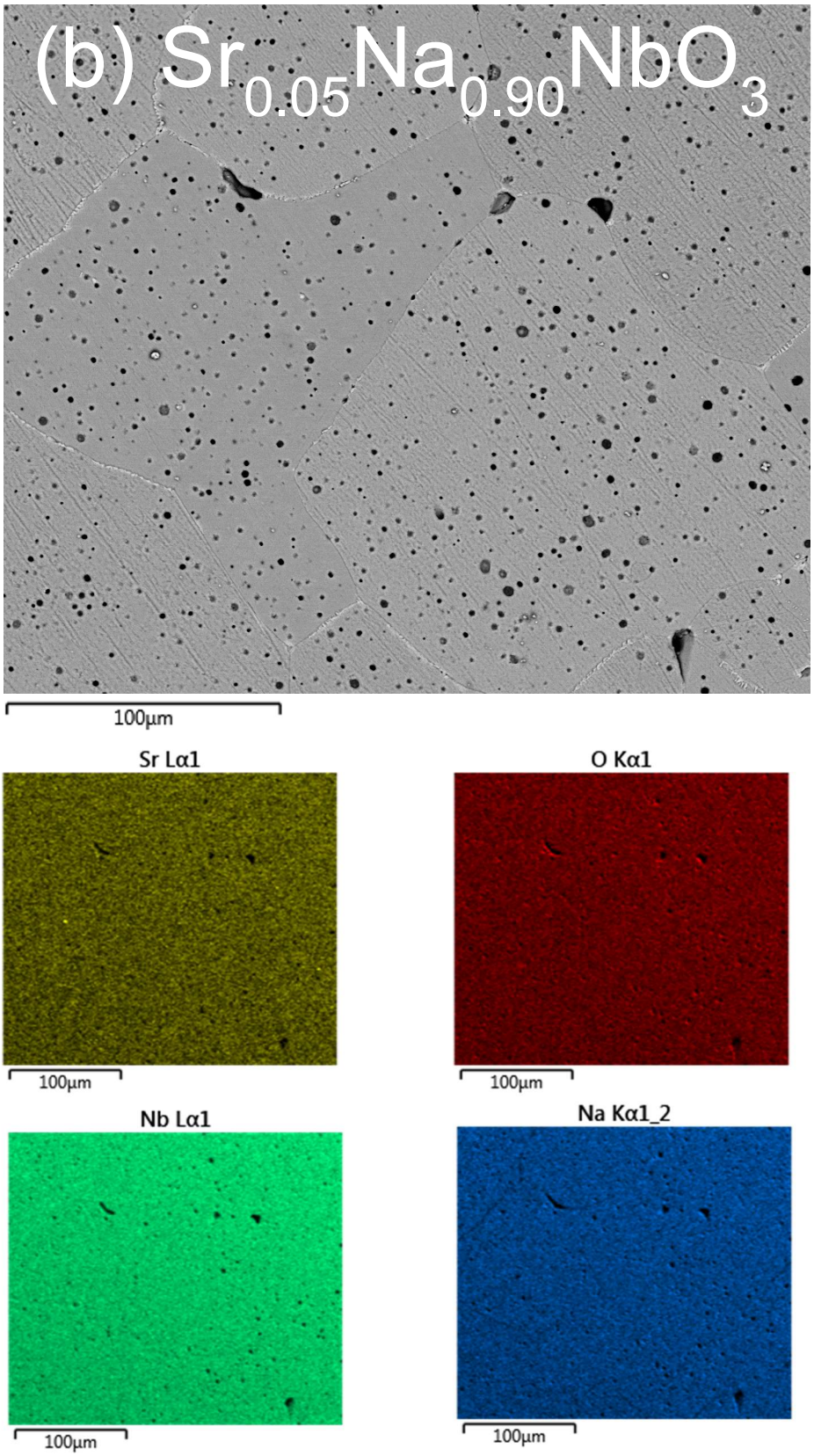
(b) $Sr_{0.05}Na_{0.90}NbO_3$
100μm
Sr Lα1
100μm
O Kα1
100μm
Nb Lα1
100μm
Na Kα1_2
100μm

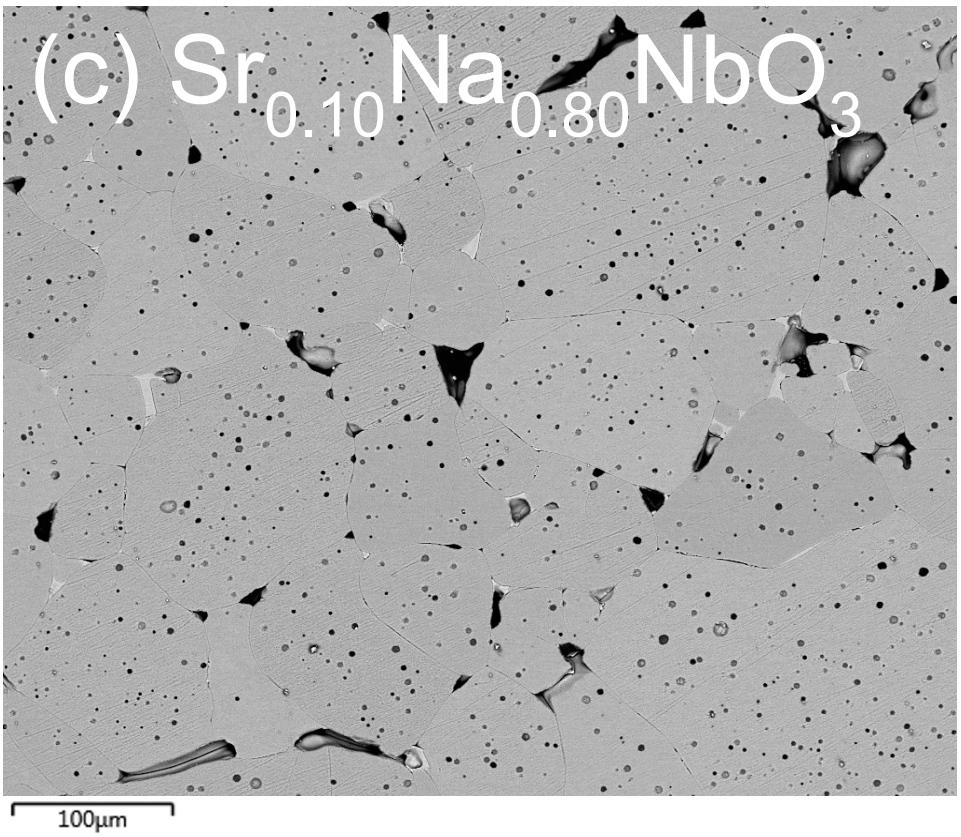
(c) $Sr_{0.10}Na_{0.80}NbO_3$
100µm

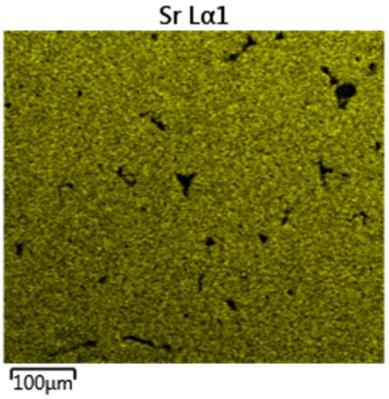
Sr Lα1
100µm

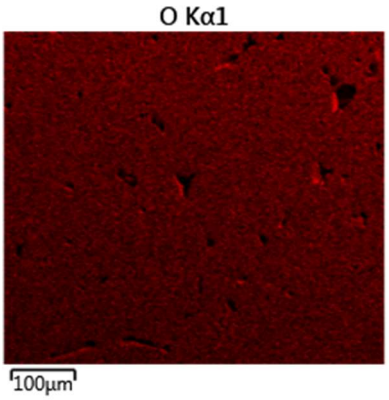
O Kα1
100µm

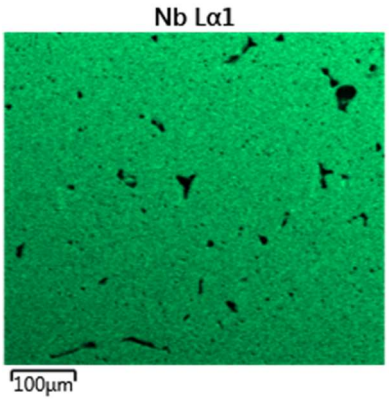
Nb Lα1
100µm

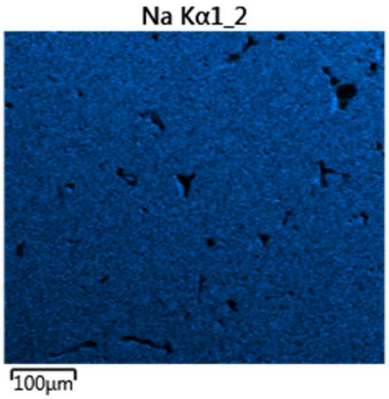
Na Kα1_2
100µm

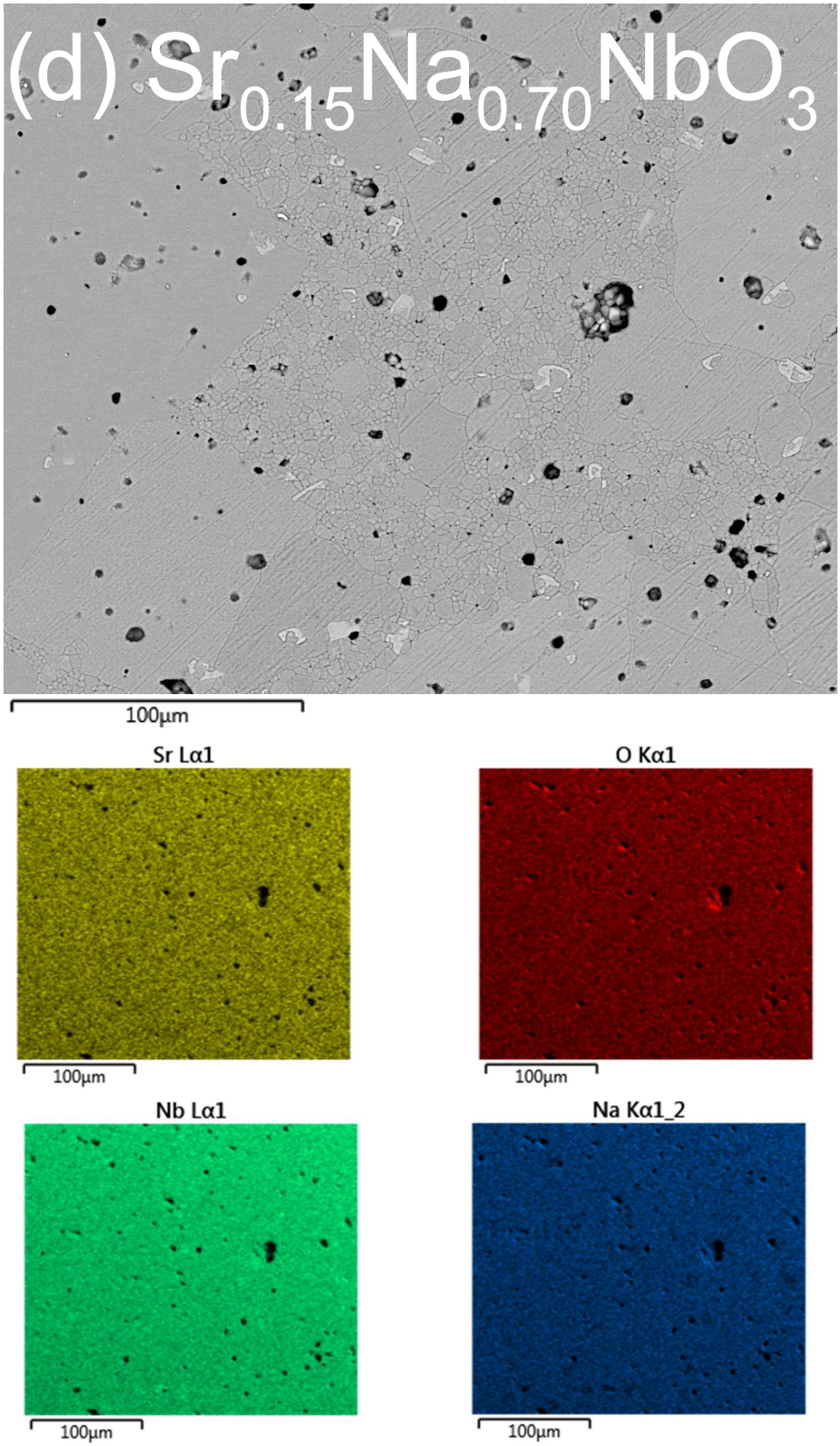
(d) $Sr_{0.15}Na_{0.70}NbO_3$
100μm
Sr Lα1
100μm
O Kα1
100μm
Nb Lα1
100μm
Na Kα1_2
100μm

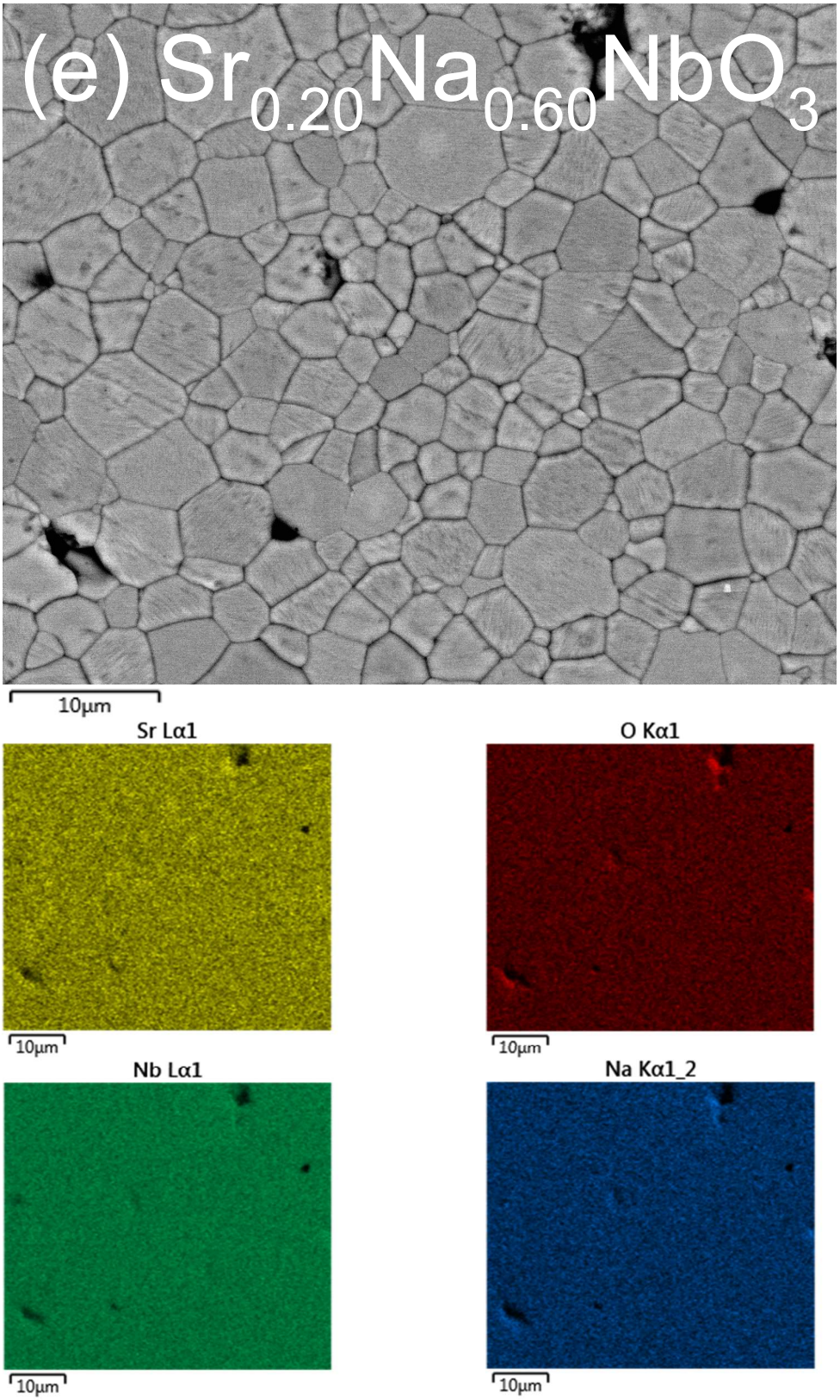
(e) $Sr_{0.20}Na_{0.60}NbO_3$
10μm
Sr Lα1
10μm
O Kα1
10μm
Nb Lα1
10μm
Na Kα1_2
10μm

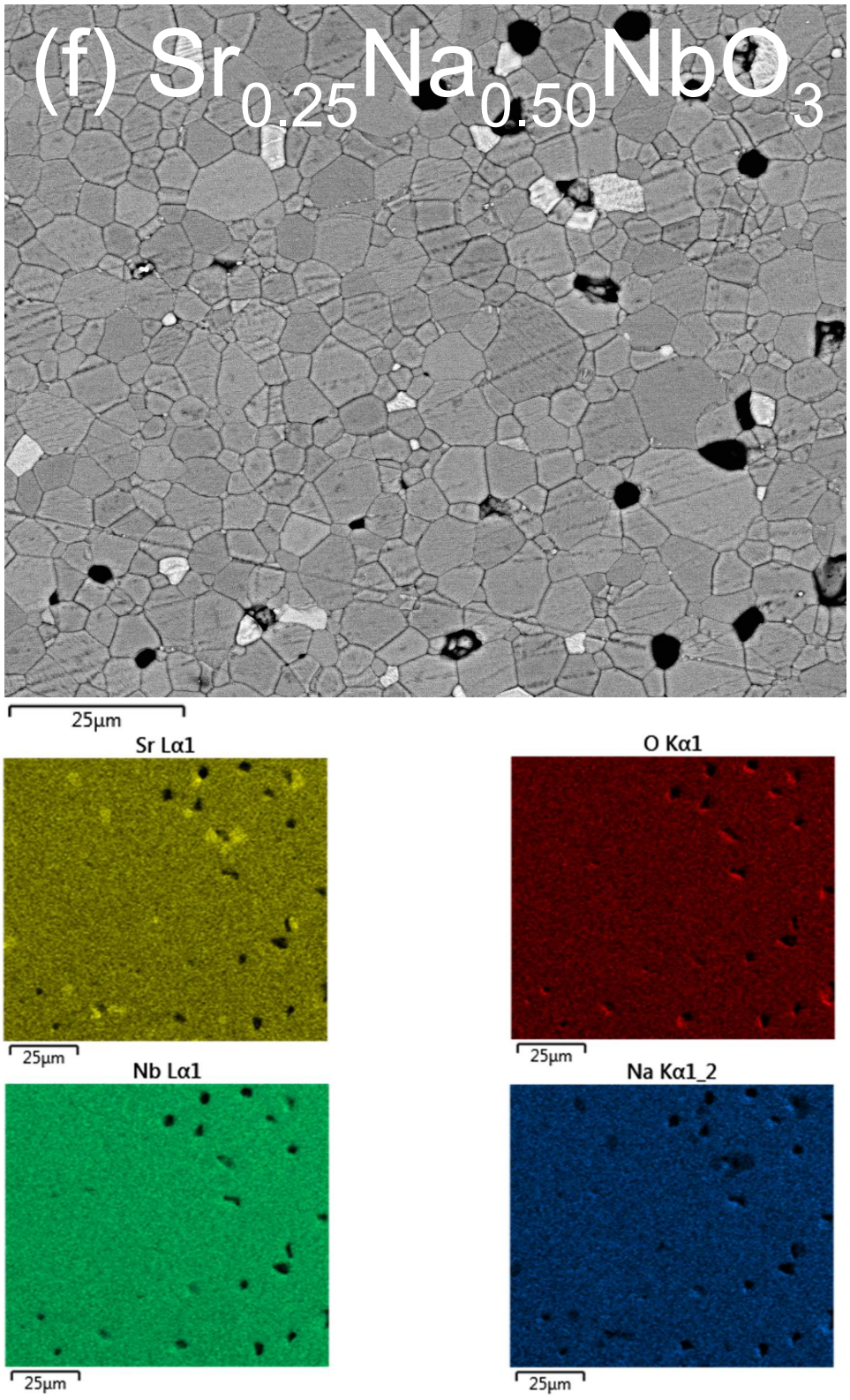

Figure S10: Backscatter electron micrographs and corresponding EDX maps of polished and thermally etched samples of (a) $NaNbO_3$, (b) $Sr_{0.05}Na_{0.90}NbO_3$, (c) $Sr_{0.10}Na_{0.80}NbO_3$, (d) $Sr_{0.15}Na_{0.70}NbO_3$, (e) $Sr_{0.20}Na_{0.60}NbO_3$, and (f) $Sr_{0.25}Na_{0.50}NbO_3$. Bright regions in (c) and (d) can be identified as $NaNb_3O_8$ and in (f) as tetragonal tungsten bronze $Sr_2NaNb_5O_{15}$

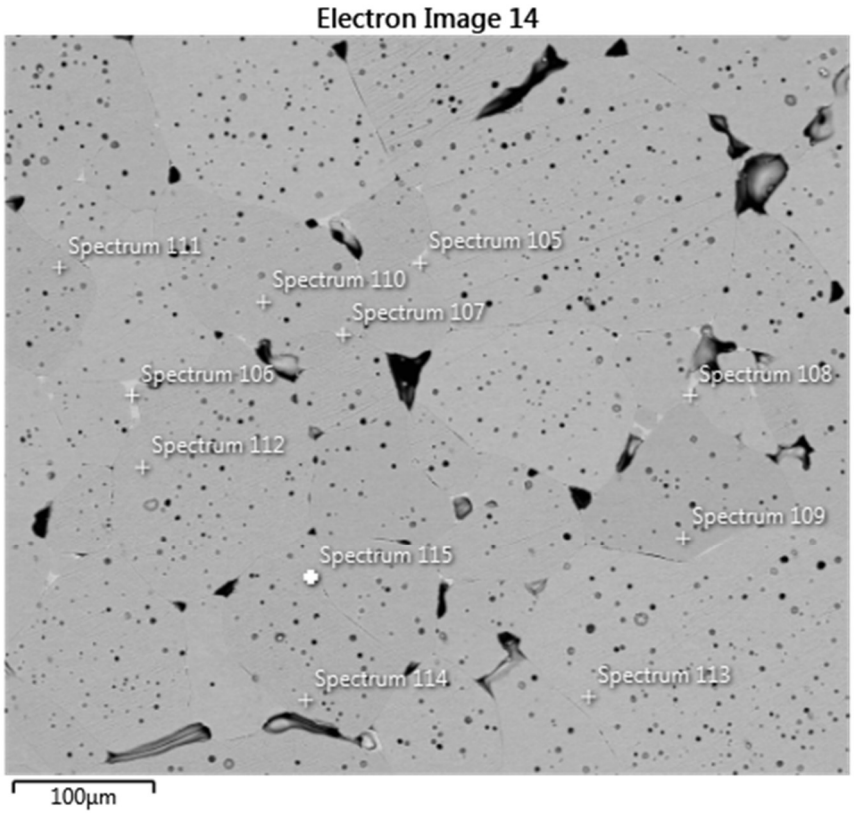

Figure S11: Backscattered electron micrograph of polished and thermally etched $Sr_{0.10}Na_{0.80}NbO_3$ bulk ceramic, annotated with point spectra positions.

Table S1: Spectrum number according to Figure S11, and corresponding atomic percentage of ions. Highlighted cells correspond to regions of bright contrast.

Spectrum	O (at%)	Na (at%)	Sr (at%)	Nb (at%)
105	63.22	8.74	0.3	27.73
106	61.53	9.08	0.47	28.93
107	62.8	9.87	0.5	26.82
108	62.43	9.01	0.18	28.39
109	57.29	16.14	2.18	24.4
110	57.53	16.59	2.1	23.78
111	58.05	15.83	2.11	24.02
112	57.17	16.67	2.13	24.03
113	57.7	16.23	2.15	23.92
114	58.74	16.23	2.06	22.96
115	57.52	15.8	2.1	24.58

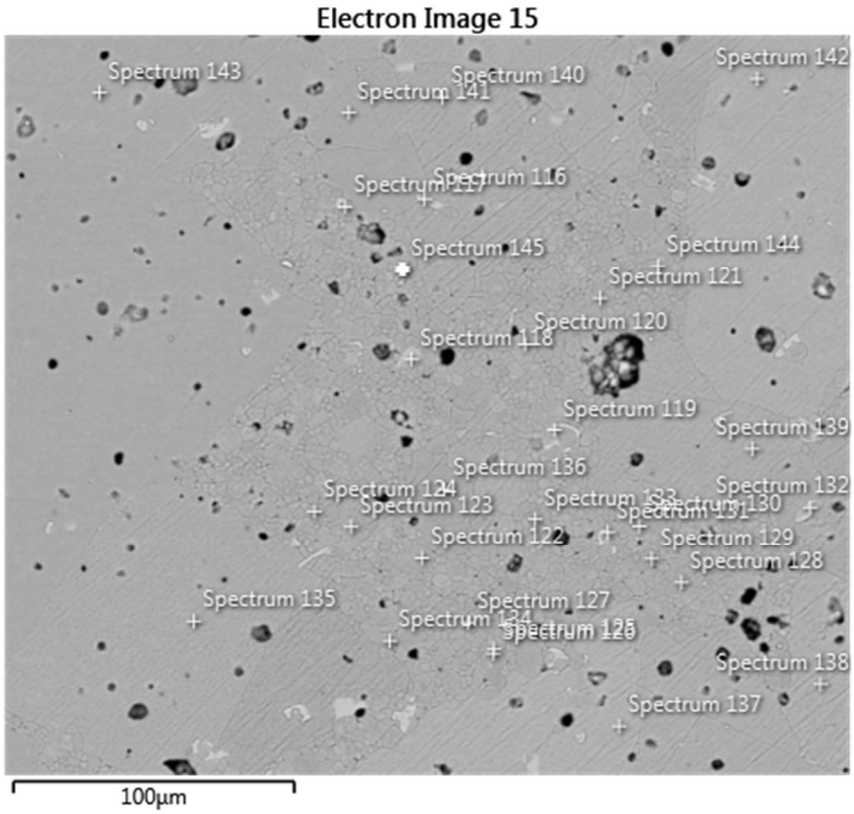

Figure S12: Backscattered electron micrograph of polished and thermally etched $Sr_{0.15}Na_{0.70}NbO_3$ bulk ceramic, annotated with point spectra positions.

Table S2: Spectrum number according to Figure S12, and corresponding atomic percentage of ions. Highlighted cells correspond to regions of bright contrast.

Spectrum	O	Na	Sr	Nb
116	63.49	7.29	1.89	27.33
117	63.3	7.59	1.8	27.32
118	62.33	7.51	1.83	28.34
119	63.21	7.46	1.79	27.55
120	58.67	14.3	3.25	23.79
121	58.56	14.28	3.18	23.98
122	58.56	14.25	3.24	24.01
123	57.84	14.53	3.07	24.56

124	57.29	14.53	3.41	24.78
125	59.72	14.55	2.91	22.82
126	58.28	14.07	3.38	24.27
127	57.96	14.33	3.21	24.51
128	58.14	14.85	3	24.01
129	58.17	14.1	3.29	24.44
130	58.36	14.3	3.19	24.15
131	64.44	8.15	1.83	25.58
132	61.88	7.43	1.97	28.72
133	59.27	13.94	3.19	23.59
134	58.47	13.93	3.32	24.28
135	58.88	13.63	3.47	24.03
136	58.27	14.13	3.28	24.32
137	59.66	14.01	3.14	23.19
138	57.49	14.33	3.21	24.97

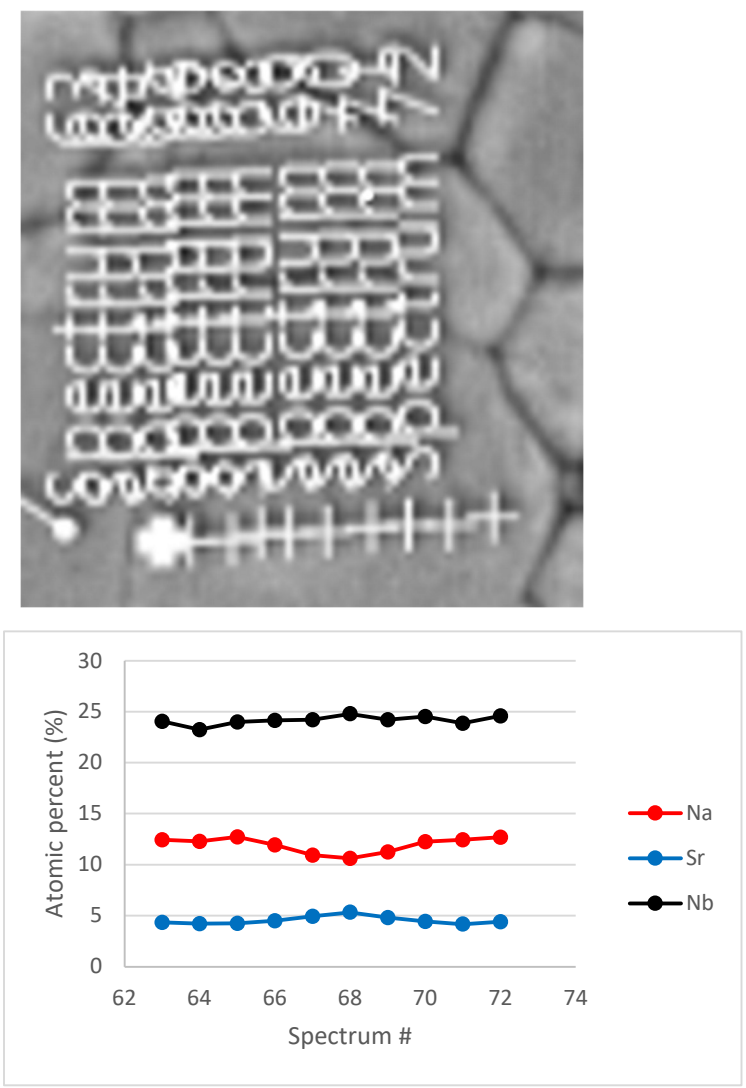

Figure S13: Point spectra across a grain in polished and thermally etched $Sr_{0.20}Na_{0.60}NbO_3$ and corresponding atomic percentage to demonstrate core-shell microstructure.

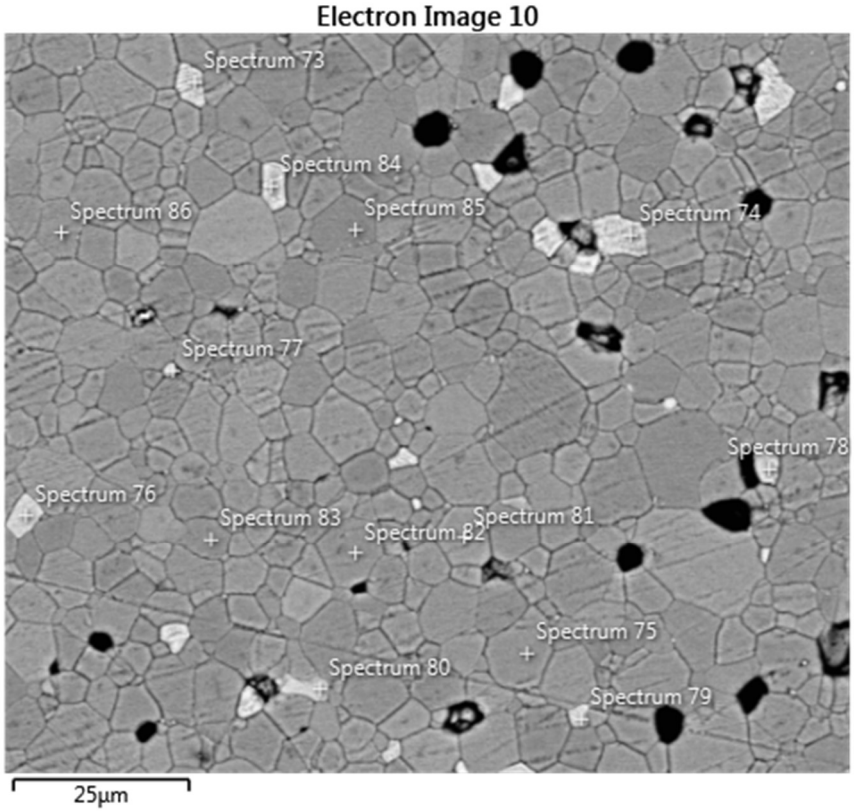

Figure S14: Backscattered electron micrograph of polished and thermally etched $Sr_{0.25}Na_{0.50}NbO_3$ bulk ceramic, annotated with point spectra positions.

Table S3: Spectrum number according to Figure S14, and corresponding atomic percentage of ions. Highlighted cells correspond to regions of bright contrast.

Spectrum	O (at%)	Na (at%)	Sr (at%)	Nb (at%)
73	61.25	4.95	8.09	25.71
74	63.05	4.28	8.36	24.32
75	58.45	10.41	5.67	25.48
76	60.43	4.13	9.02	26.42
77	44.97	9.85	7.68	37.5
78	59.76	4.55	8.88	26.82
79	61.37	5.25	8.03	25.35

80	60.47	5.34	7.96	26.23
81	59.34	10.31	5.58	24.77
82	58.85	10.56	5.64	24.95
83	58.84	10.35	5.59	25.22
84	60.53	4.29	9.14	26.05
85	58.28	10.69	5.7	25.33
86	59.3	10.38	5.63	24.69

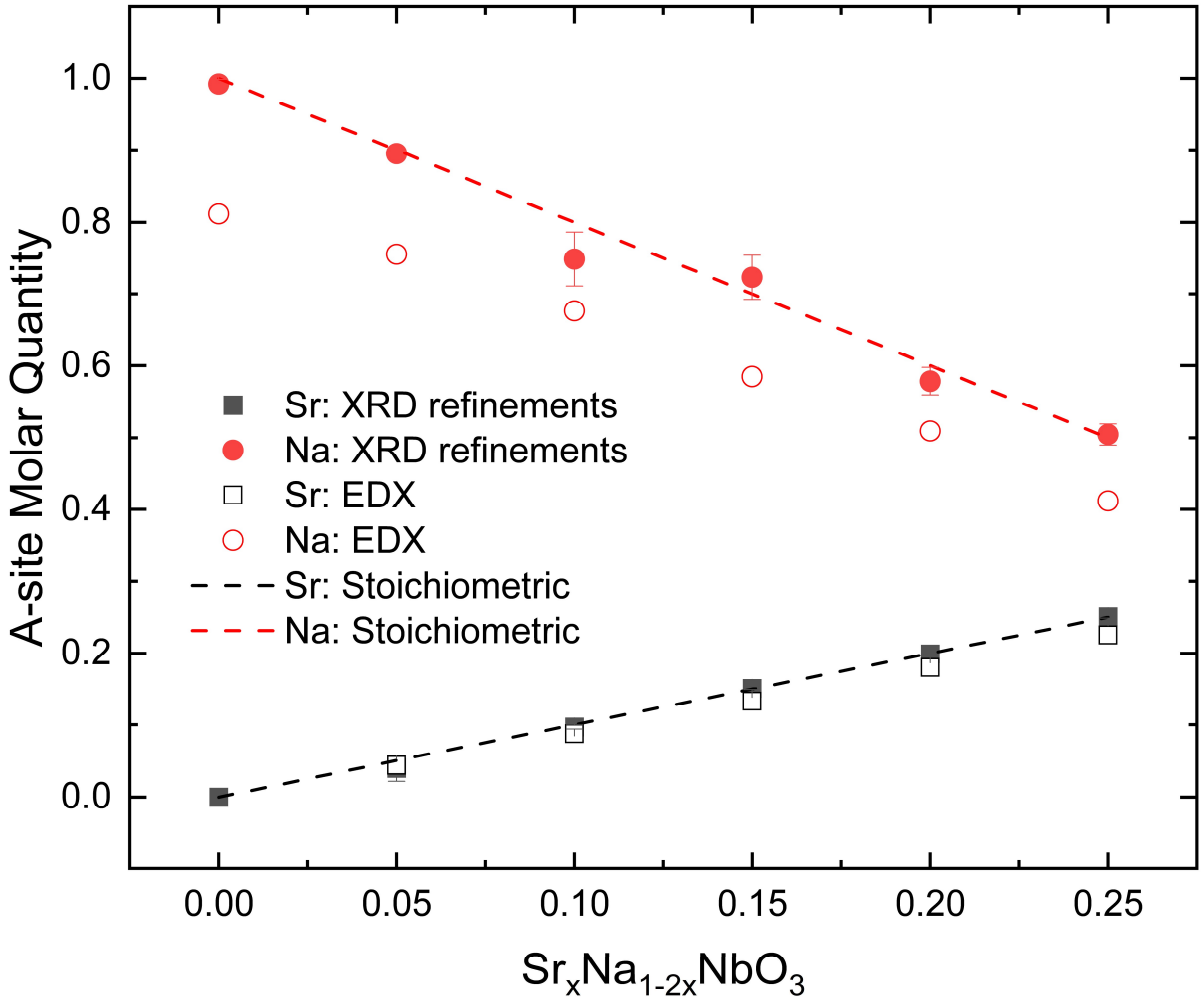

Figure S15: Sr^{2+} and Na^{+} occupancies extracted from Rietveld refinements (solid data points) and average at% calculated from EDX mapping (hollow data points) against composition. Dashed lines correspond to nominal $Sr_xNa_{1-2x}NbO_3$

SI Section S5: Dielectric Spectroscopy

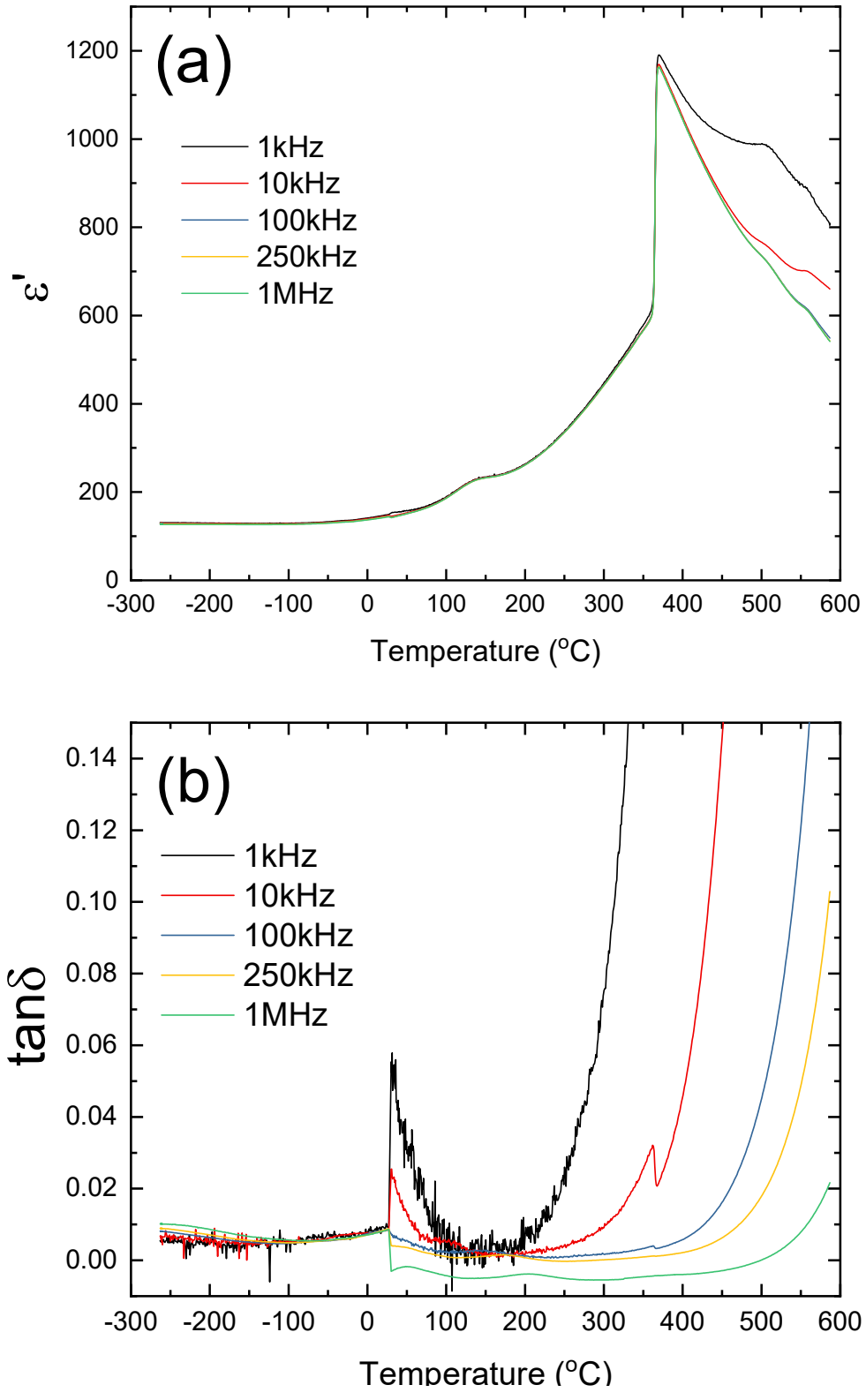

Figure S16: (a) Real component of permittivity (ε') and (b) tan δ at fixed frequencies against temperature for $NaNbO_3$ (x = 0.00). Sub-zero tan δ are due to electrical noise (inductance) from electrical testing equipment.

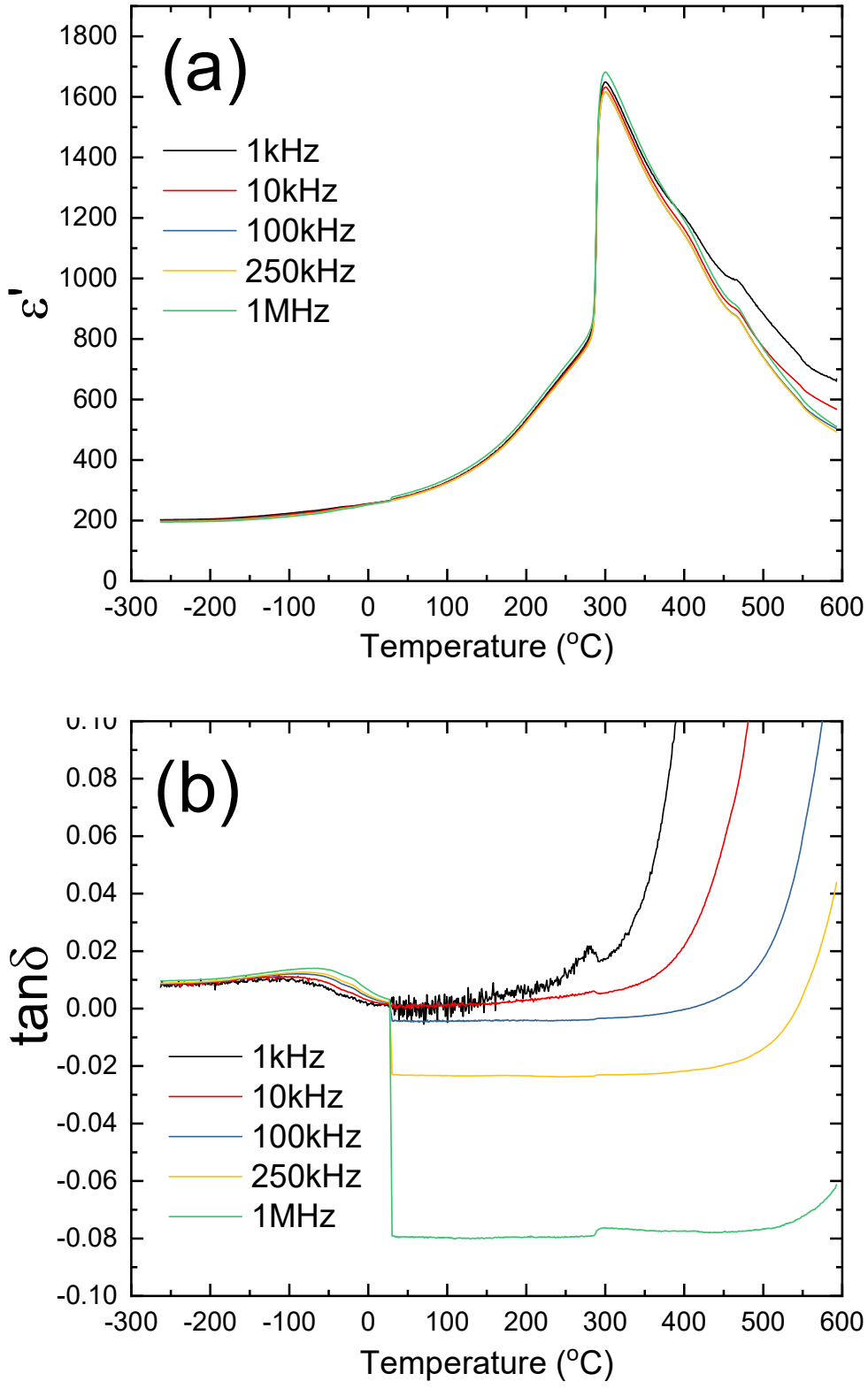

Figure S17: (a) Real component of permittivity (ε') and (b) tan δ at fixed frequencies against temperature for $Sr_{0.05}Na_{0.90}NbO_3$ (x = 0.05). Sub-zero tan δ are due to electrical noise (inductance) from electrical testing equipment.

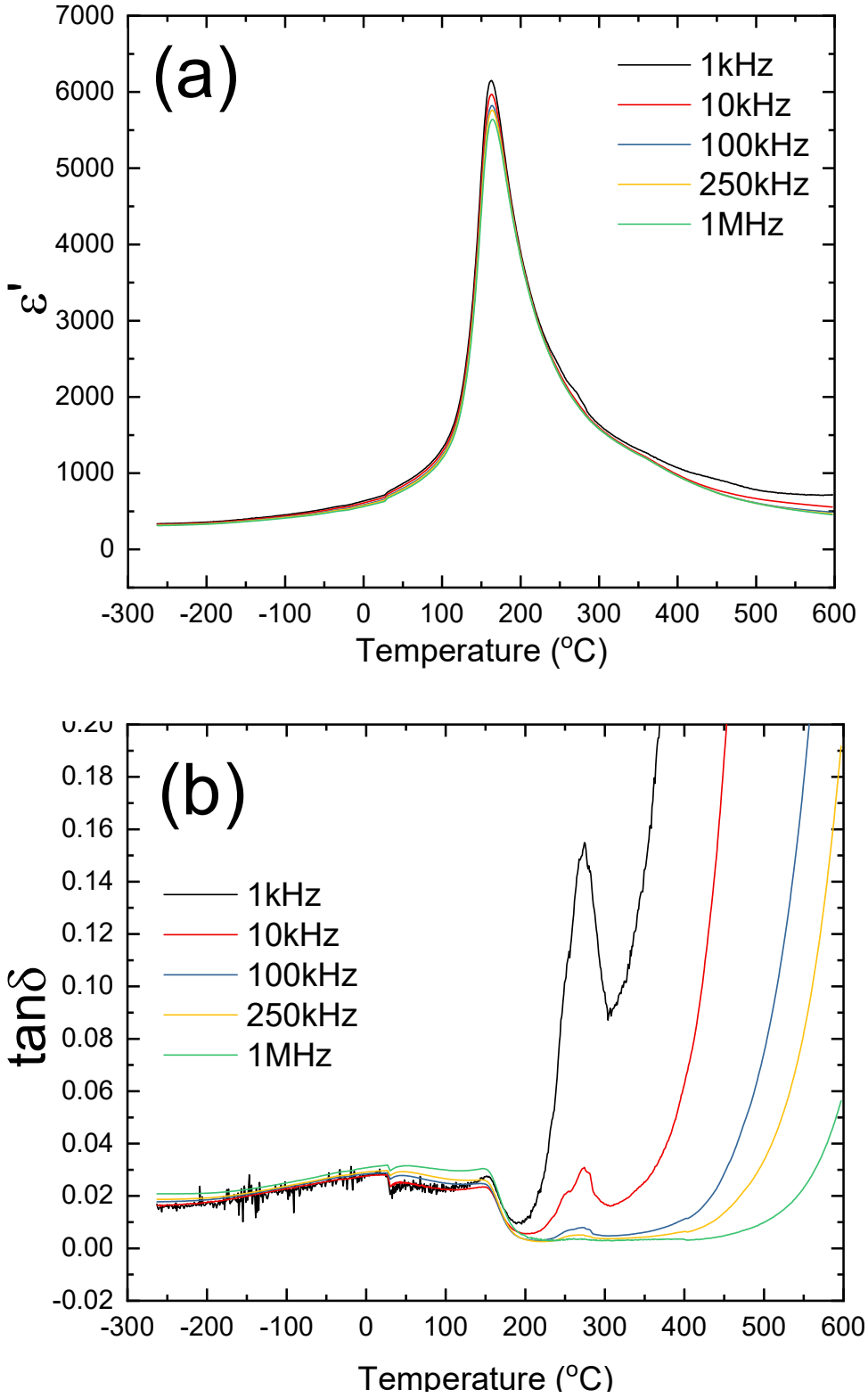

Figure S18: (a) Real component of permittivity (ε') and (b) tan δ at fixed frequencies against temperature for $Sr_{0.10}Na_{0.80}NbO_3$ (x = 0.10)

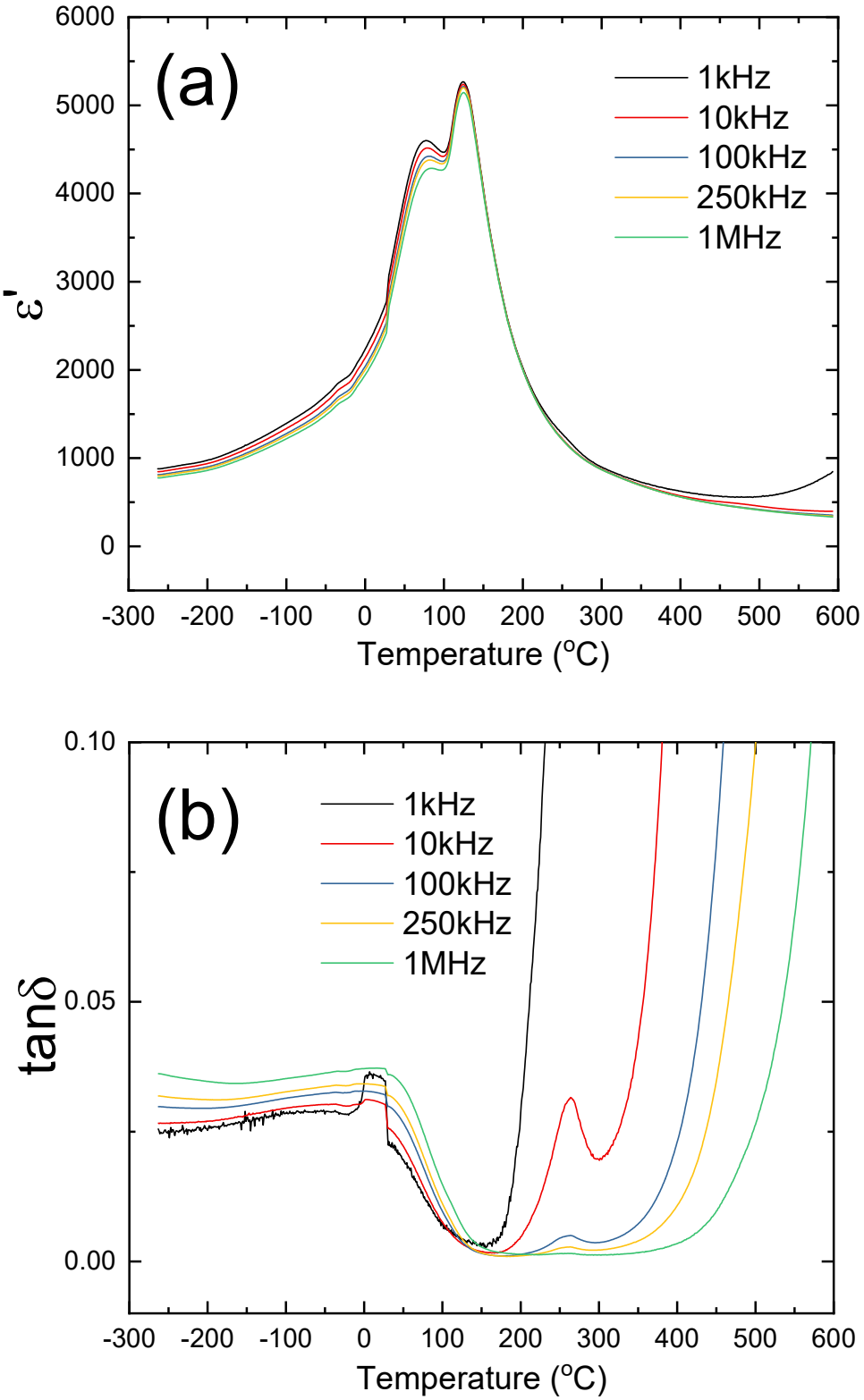

Figure S19: (a) Real component of permittivity (ε') and (b) tan δ at fixed frequencies against temperature for $Sr_{0.15}Na_{0.70}NbO_3$ (x = 0.15)

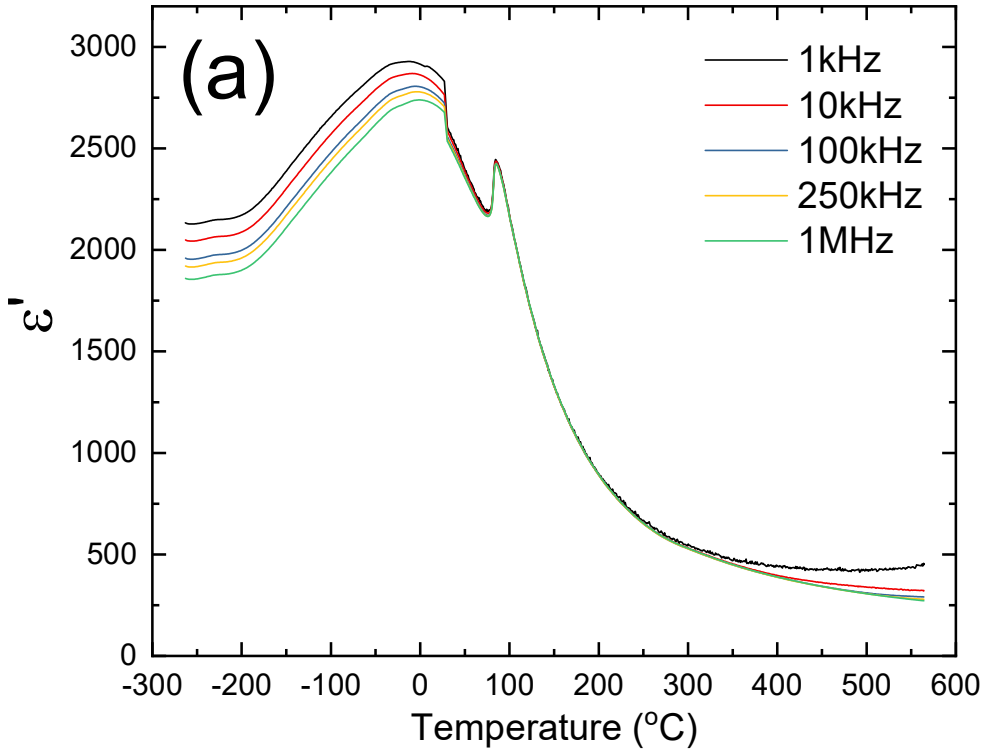

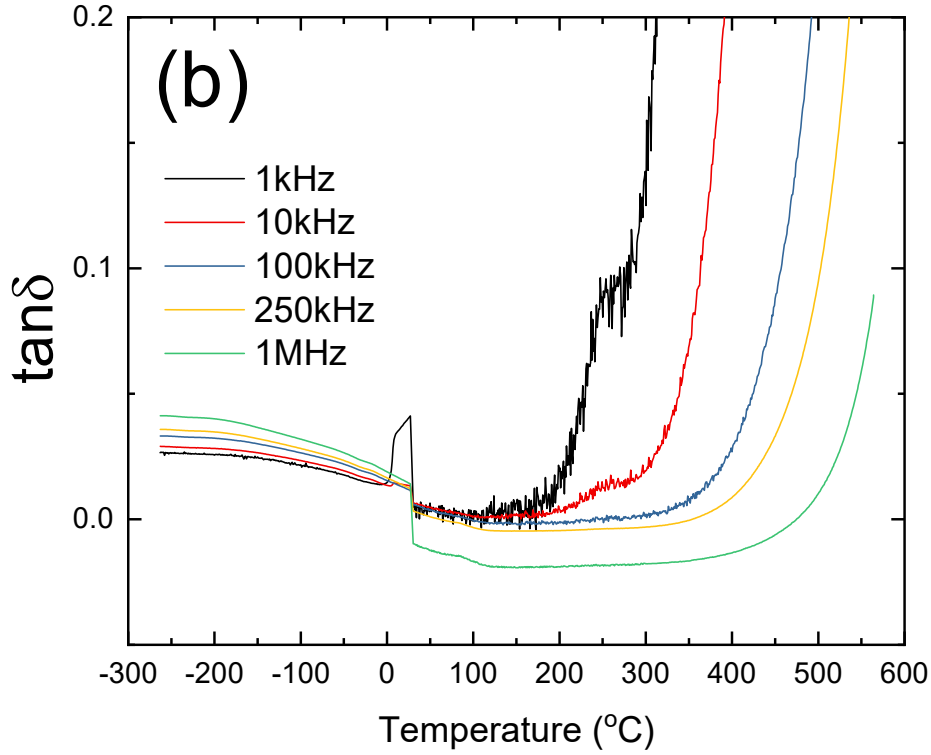

Figure S20: (a) Real component of permittivity (ε') and (b) tan δ at fixed frequencies against temperature for $Sr_{0.20}Na_{0.60}NbO_3$ (x = 0.20). Sub-zero tan δ are due to electrical noise (inductance) from electrical testing equipment.

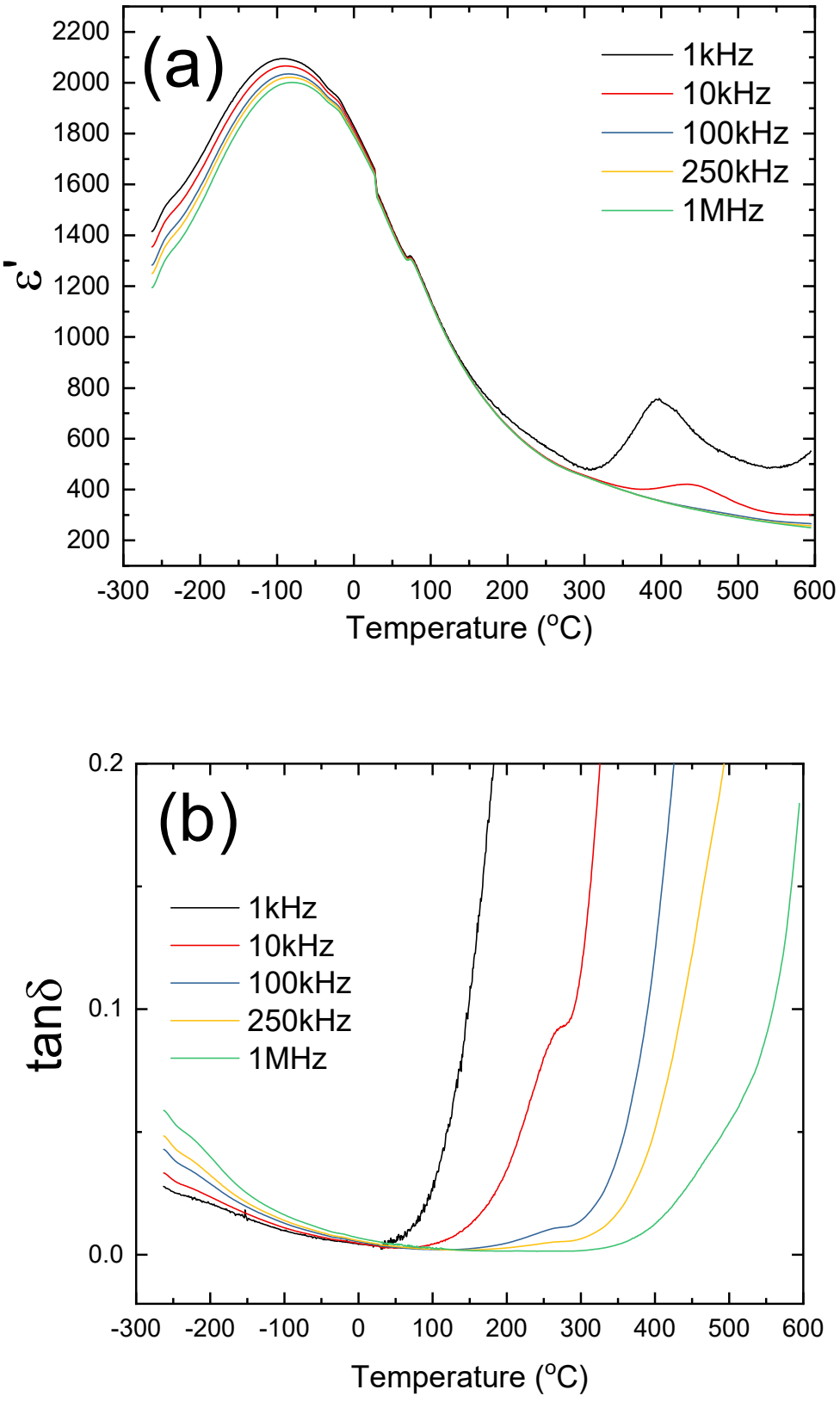

Figure S21: (a) Real component of permittivity (ε') and (b) tan δ at fixed frequencies against temperature for $Sr_{0.25}Na_{0.50}NbO_3$ (x = 0.25)

SI Section S6: Polarisation vs Electric Field analysis

Table S4: Maximum polarisation (P_{max}), remnant polarisation (P_R), coercive filed (E_C), recoverable energy density (W_{rec}), energy loss density (W_{loss}), thickness (S) over electrode radius (r), and efficiency ($W_{rec}/W_{rec}+W_{loss}$) for $Sr_xNa_{1-2x}NbO_3$ (x = 0.00, 0.05, 0.10, 0.15, 0.20, 0.25) at 40 $kV.cm^{-1}$

$Sr_xNa_{1-2x}NbO_3$	P_{max} ($\mu C.cm^{-2}$)	P_R ($\mu C.cm^{-2}$)	E_C ($kV.cm^{-1}$)	W_{rec} ($mJ.cm^{-3}$)	W_{loss} ($mJ.cm^{-3}$)	S/r	η (%)
0	1.03	0.31	9.94	12.4	16.5	0.34	42.9
0.05	1.49	0.37	9.90	20.5	22.3	0.36	47.8
0.1	6.63	4.60	17.58	25.3	120.3	0.37	17.4
0.15	14.19	6.43	8.01	100.5	162.9	0.35	38.2
0.20	9.63	0.30	1.60	173.4	20.9	0.45	89.2
0.25	6.57	2.04	11.85	71.4	96.7	0.42	42.5

SI Section S7: Impedance Spectroscopy and Arrhenius plots

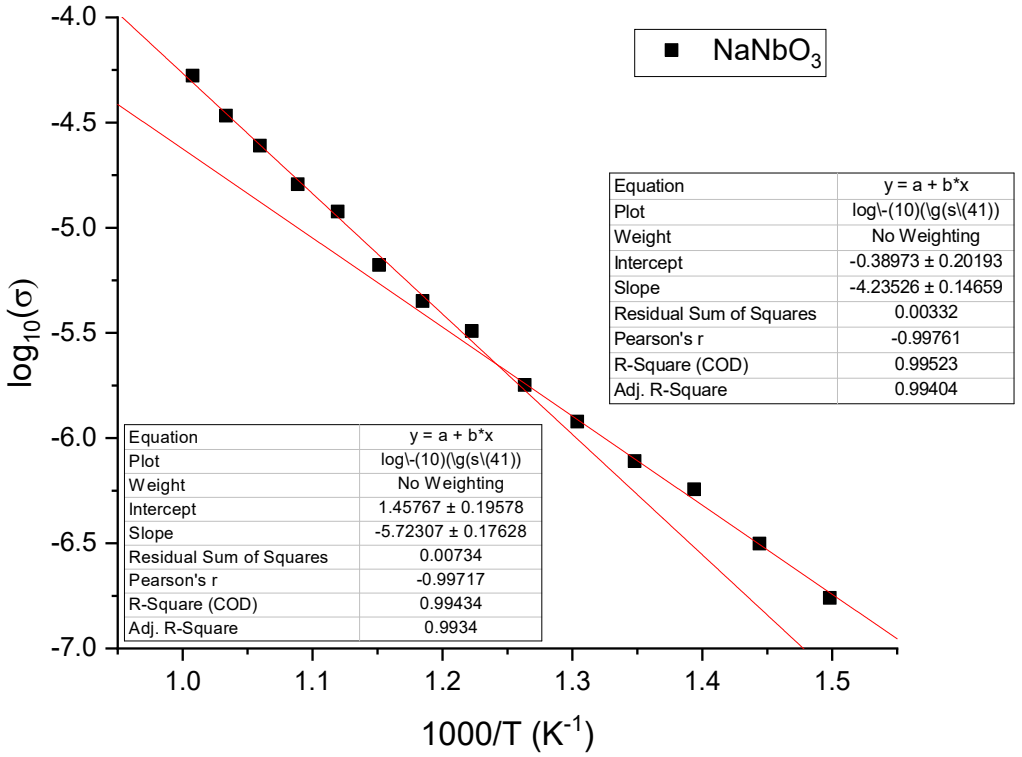

Equation	y = a + b*x
Plot	log\-(10)(\g(s\(41))
Weight	No Weighting
Intercept	-0.38973 ± 0.20193
Slope	-4.23526 ± 0.14659
Residual Sum of Squares	0.00332
Pearson's r	-0.99761
R-Square (COD)	0.99523
Adj. R-Square	0.99404

Equation	y = a + b*x
Plot	log\-(10)(\g(s\(41))
Weight	No Weighting
Intercept	1.45767 ± 0.19578
Slope	-5.72307 ± 0.17628
Residual Sum of Squares	0.00734
Pearson's r	-0.99717
R-Square (COD)	0.99434
Adj. R-Square	0.9934

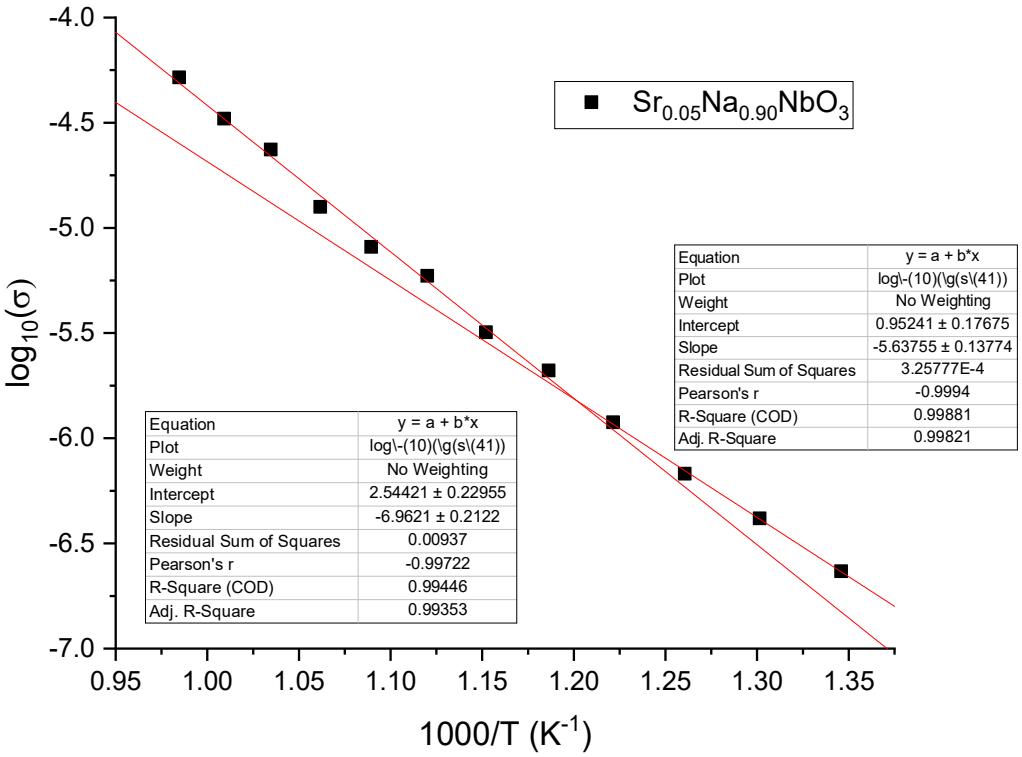

Equation	y = a + b*x
Plot	log\-(10)(\g(s\(41))
Weight	No Weighting
Intercept	0.95241 ± 0.17675
Slope	-5.63755 ± 0.13774
Residual Sum of Squares	3.25777E-4
Pearson's r	-0.9994
R-Square (COD)	0.99881
Adj. R-Square	0.99821

Equation	y = a + b*x
Plot	log\-(10)(\g(s\(41))
Weight	No Weighting
Intercept	2.54421 ± 0.22955
Slope	-6.9621 ± 0.2122
Residual Sum of Squares	0.00937
Pearson's r	-0.99722
R-Square (COD)	0.99446
Adj. R-Square	0.99353

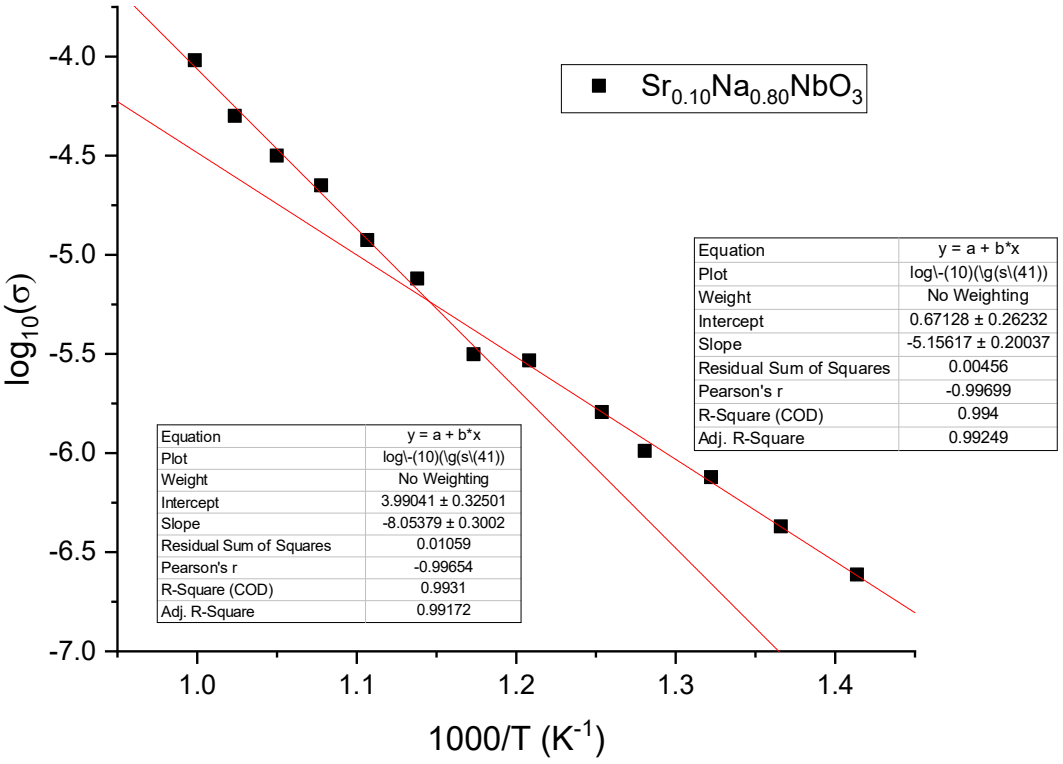
Sr0.10Na0.80NbO3
log10(σ)
1000/T (K-1)
-4.0
-4.5
-5.0
-5.5
-6.0
-6.5
-7.0
1.0
1.1
1.2
1.3
1.4
Equation y = a + b*x
Plot log\-(10)(\g(s\(41))
Weight No Weighting
Intercept 0.67128 ± 0.26232
Slope -5.15617 ± 0.20037
Residual Sum of Squares 0.00456
Pearson's r -0.99699
R-Square (COD) 0.994
Adj. R-Square 0.99249
Equation y = a + b*x
Plot log\-(10)(\g(s\(41))
Weight No Weighting
Intercept 3.99041 ± 0.32501
Slope -8.05379 ± 0.3002
Residual Sum of Squares 0.01059
Pearson's r -0.99654
R-Square (COD) 0.9931
Adj. R-Square 0.99172

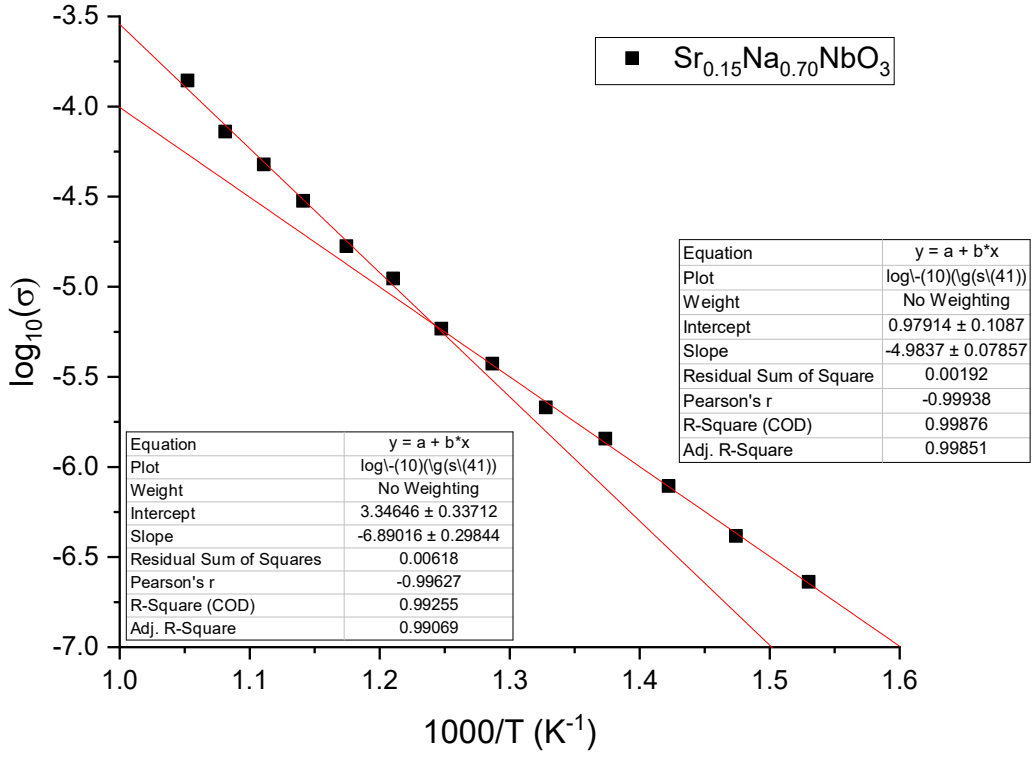
Sr0.15Na0.70NbO3
log10(σ)
1000/T (K-1)
-3.5
-4.0
-4.5
-5.0
-5.5
-6.0
-6.5
-7.0
1.0
1.1
1.2
1.3
1.4
1.5
1.6
Equation y = a + b*x
Plot log\-(10)(\g(s\(41))
Weight No Weighting
Intercept 0.97914 ± 0.1087
Slope -4.9837 ± 0.07857
Residual Sum of Square 0.00192
Pearson's r -0.99938
R-Square (COD) 0.99876
Adj. R-Square 0.99851
Equation y = a + b*x
Plot log\-(10)(\g(s\(41))
Weight No Weighting
Intercept 3.34646 ± 0.33712
Slope -6.89016 ± 0.29844
Residual Sum of Squares 0.00618
Pearson's r -0.99627
R-Square (COD) 0.99255
Adj. R-Square 0.99069

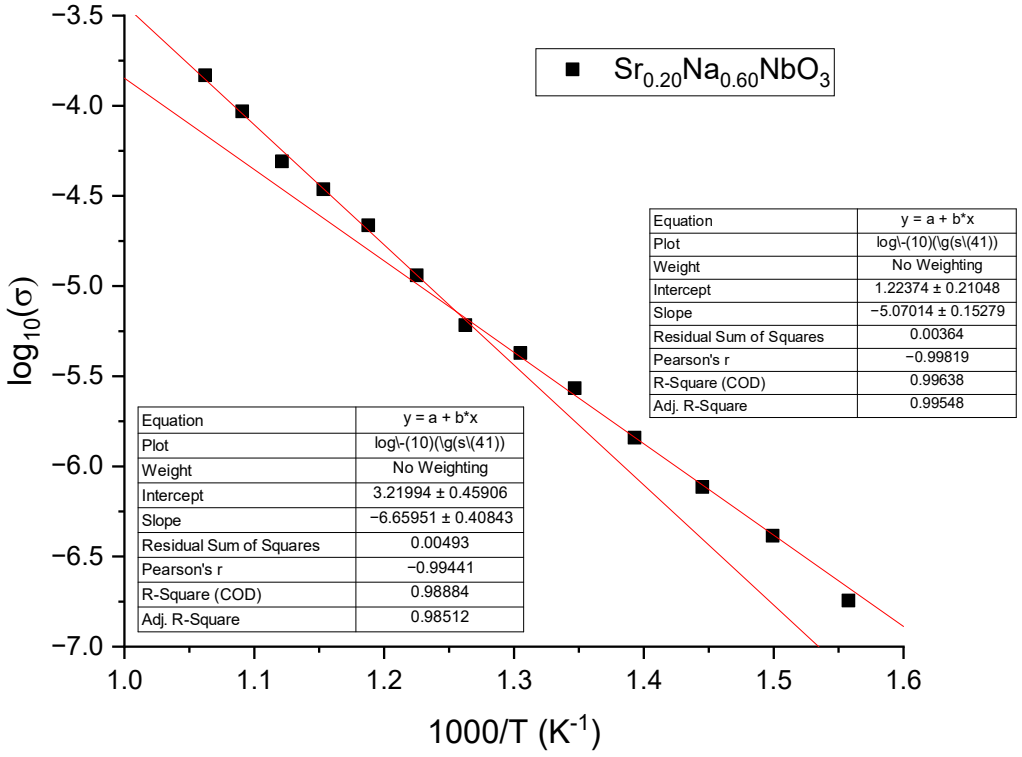

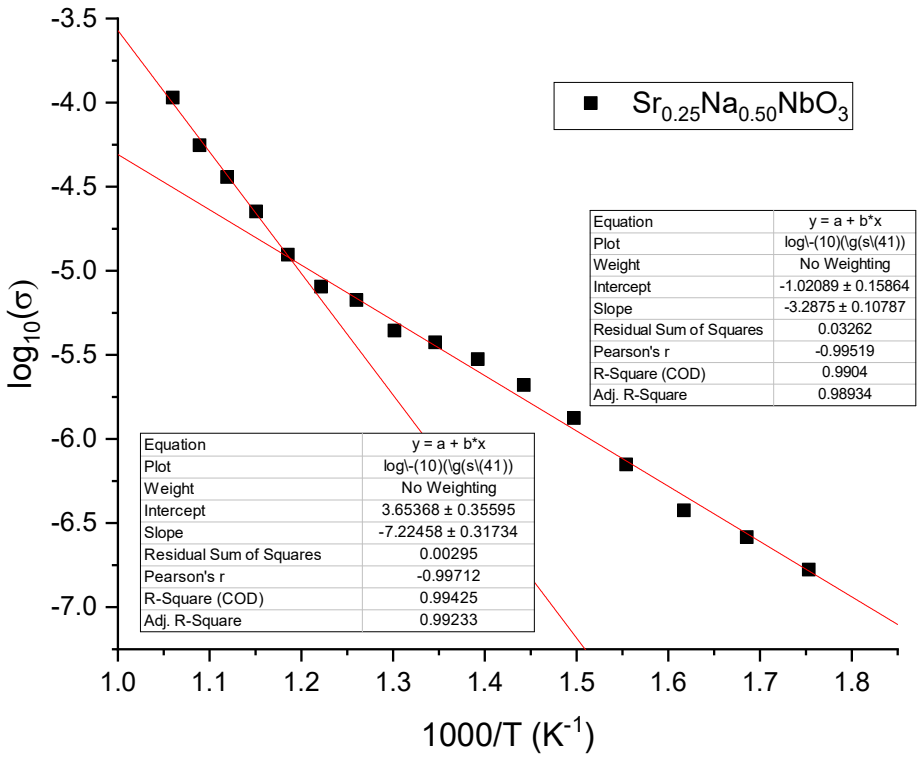

Figure S22: Arrhenius plots of conductivity calculated using M'' at the relaxation frequency for (a) $NaNbO_3$, (b) $Sr_{0.05}Na_{0.90}NbO_3$, (c) $Sr_{0.10}Na_{0.80}NbO_3$, (d) $Sr_{0.15}Na_{0.70}NbO_3$, (e) $Sr_{0.20}Na_{0.60}NbO_3$, and (f) $Sr_{0.25}Na_{0.50}NbO_3$.

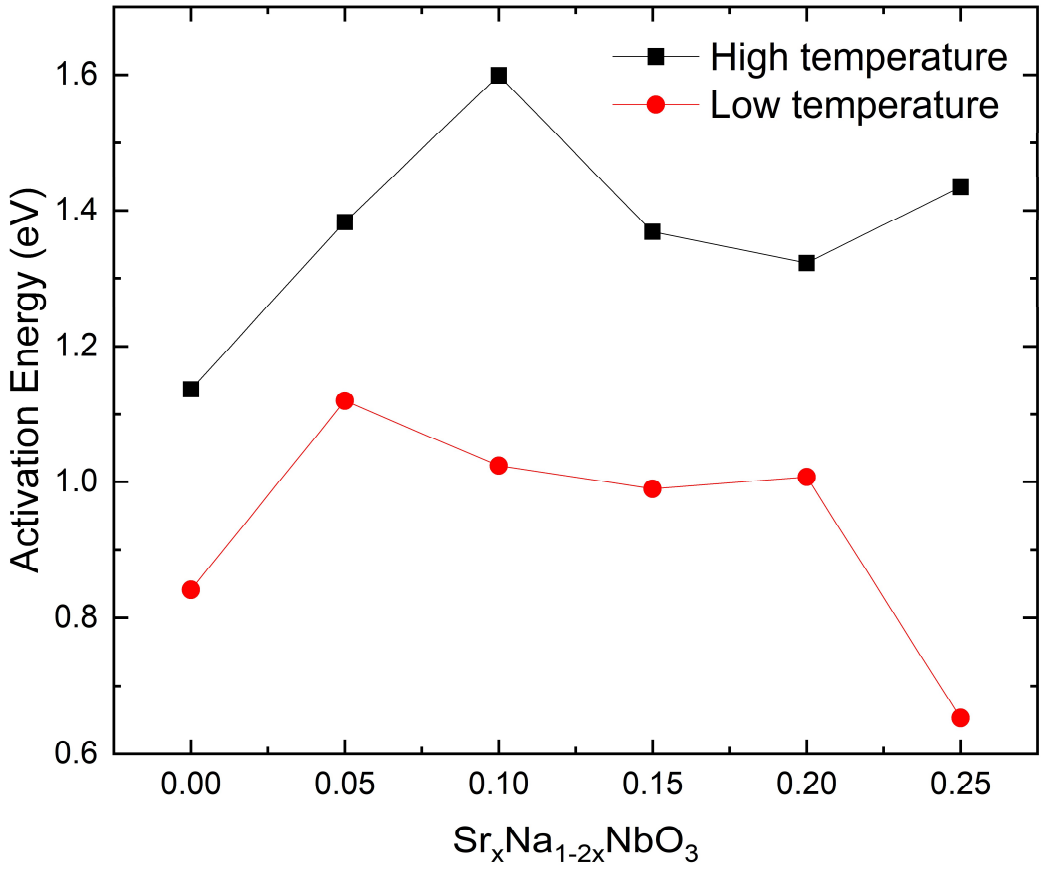

Figure S23: High temperature and low temperature activation energies extrapolated from Arrhenius plots of conductivity against composition.